Mg-1Zn-1Ca alloy for biomedical applications. Influence of the secondary phases on the mechanical and corrosion behaviour.

N. Pulido-González[a], B. Torres[a,*], S. García-Rodríguez[a], P. Rodrigo[a], V. Bonache[a], P. Hidalgo-Manrique[a], M. Mohedano[b], J. Rams[a]

[a] *Departamento de Matemática Aplicada, Ciencia e Ingeniería de Materiales y Tecnología Electrónica, ESCET, Universidad Rey Juan Carlos, C/ Tulipán s/n, 28933, Móstoles, Madrid, Spain*

[b] *Departamento de Ciencia de Materiales, Facultad de Ciencias Químicas, Universidad Complutense, 28040 Madrid, Spain*

Abstract

An as-cast Mg-1Zn-1Ca alloy has been soundly characterized to be used as a biodegradable material in biomedical applications. Ca and Zn additions have a great influence in the microstructure, mechanical properties and corrosion behaviour of Mg alloys. SEM examinations revealed that most of the Ca and Zn atoms form Mg_2Ca and $Ca_2Mg_6Zn_3$ precipitates, which distribute preferentially along the grain boundaries forming a continuous network of secondary phases. The results of nanoindentation tests show differences in hardness and elastic modulus between the α-Mg matrix and the secondary phases. The results of three-point bending tests shows that cracks propagate following the network formed by the intermetallic compounds at the grain boundaries (GBs). The evolved hydrogen after immersion in Hank's solution of the alloy has been also estimated, showing a change in the corrosion mechanism after 160 h. The intermetallic compounds act as a barrier against corrosion, so that it progresses through the α-Mg matrix phase.

Keywords

Mg-Zn-Ca alloys; Biomaterials; Biodegradable implants; Three-point bending test; Nanoindentation; Corrosion behaviour

1. Introduction

Magnesium (Mg) alloys are being studied as promising biodegradable materials for orthopedic applications since they exhibit low density, mechanical properties close to those of natural bone and some attractive properties such as biocompatibility, bioactivity and osseointegration. Biodegradable materials can degrade or be absorbed into the human body avoiding an unnecessary second surgery to remove them after the complete bone healing [1,2]. However, Mg alloys present a poor corrosion resistance in aqueous medium due to its great activity. From their degradation process, magnesium hydroxide ($Mg(OH)_2$) is formed as corrosion product and hydrogen bubbles evolve, which cause a rise in the pH of the surrounding areas and could produce swelling within the body. The composition design is considered as an effective tool to improve the corrosion resistance of Mg and its alloys [3–7]. In the biomedical field, alloying elements must be non-toxic for the organism and preferably appear naturally in the human body. Gu et al. [8] found that Zn and Ca were suitable alloying elements for orthopedic implants: Ca is the main constituent of the bone, favouring their formation and growth, and Zn is one of the principal nutrients in the organism [9–11]. Bakhsheshi-Rad et al. [4,9,12] performed different studies on Mg-1Ca-xZn alloys and they found that the corrosion potential decreases by increasing the Zn content from 0.5 to 1.25 - 1.5 wt.% , but further additions of Zn (up to 4 wt.%) increase the corrosion rates. S. A. Abdel-Gawad et al. [13] established that Zn additions can improve the corrosion behaviour of the Mg-Zn-Ca system because of the formation of the $Ca_2Mg_6Zn_3$ intermetallic compound. Some authors [7,14] determined that Ca contents close to or above the solubility limit in Mg (1.35 wt.%) cause a considerable increase of the corrosion rate due to the precipitation of the brittle Mg_2Ca phase.

Particularly, the alloy containing 1 wt.% of Ca and 1 wt.% of Zn has been studied by several authors. L. Katsarou et al. [15] found that the Mg-1Zn-1Ca alloy was formed by α-Mg, and Mg_2Ca

and $Ca_2Mg_6Zn_3$ at grain boundaries and they performed hardness and creep tests as well as electrochemical corrosion tests in 0.5 wt.% NaCl but they did not evaluate this alloy in the conditions required to study it as a biomaterial. B. Zhang et al. [16] investigated this alloy and they showed that the same composition with different microstructure may show a different behaviour. S. Baek et al. [17] studied the effect of the secondary phases on the tensile behaviour of the Mg-1Zn-1Ca alloy using micro-digital image correlation to identify crack initiation. H. Wang et al. [18] investigated the Mg-1Zn-1Ca alloy coated by Ca-deficient hydroxyapatite but they did not consider the effect of the microstructure or other corrosion or mechanical properties. D. Kim et al. [19] studied the texture evolution in Mg-1Zn-1Ca alloy sheets. Y. Ortega et al. [20], X. Gao et al. [21] and M. Bamberger et al. [22] investigated the precipitation hardening of Mg-1Zn-1Ca alloys. N. Li et al. [23] showed some properties referred to Mg-1Zn-1Ca alloy compared to other Mg-based alloys by referring to other works. Finally, K. P. Rao et al. [24] tested the Mg-1Zn-1Ca alloy to evaluate its compressive strength between 25 °C and 250 °C, and workability in the range of 260 – 500 °C. In most of these studies, the authors either did not consider the microstructure distribution or used a treatment that formed a microstructure in which precipitates were not preferably placed at the grain boundaries.

On the other hand, alloys with similar composition but manufactured by different processes can have different microstructures and show strong differences in their mechanical properties and corrosion behaviour [9,10,25–32], [33]. Volume fraction, distribution, morphology and composition of secondary phases constitute the main factors affecting microstructure, mechanical properties and corrosion behaviour. For this reason, it is necessary to evaluate all of them.

In this work a complete study of a Mg-1 wt.% Zn-1 wt.% Ca (hereafter Mg-1Zn-1Ca) alloy manufactured by casting has been developed. The relationship between microstructure,

mechanical properties and corrosion behaviour of the Mg-1 wt.% Zn-1 wt.% Ca alloy has been also established. The microstructure and composition of this alloy have been thoroughly characterized in order to get a greater understanding of this alloy. In order to determine the mechanical properties, hardness tests at the nanoscale and in-situ three-point bending tests were performed, particularly because this condition is the most critical in biomedical implants. Finally, the corrosion mechanism of the alloy in Hank's solution (a standard culture medium used in biomedical research) has been established in detail. A good agreement between mechanical properties and corrosion behaviour is essential in materials developed to be used in biomedical applications, where load-bearing characteristics and an adequate corrosion rate are expected for the complete bone healing time.

2. Materials and Methods

2.1. Materials

A Mg-1 wt.% Zn-1 wt.% Ca alloy was cast by permanent mould indirect chill casting and supplied by Helmholtz Zentrum Geesthacht. Mg ingots were melted under protective atmosphere of argon with 0.2 vol.% SF_6 and held at 720 °C, being Ca and Zn added afterwards. To achieve homogeneity, the mixture was stirred for 5 min and poured into a mould. The details of the casting process can be found elsewhere [34]. Table 1 shows the composition of this alloy, which was supplied as plates with the following dimensions: 30 x 25 x 2.5 mm^3.

Table 1. Compositional analysis of the as-cast Mg-1Zn-1Ca alloy.

Element	Ca	Zn	Fe	Cu	Ni	Mg
wt. %	1.47	1.01	0.0071	0.0015	0.0007	Bal.

2.2. Composition and Microstructure Characterization

X-ray diffraction (XRD) technique was used to determine the crystalline phases of the alloy. A Panalytical X'Pert PRO diffractometer was employed using monochromatic KαCu (1.54056 Å) as the radiation source, operating at a voltage of 40 kV and a current of 40 mA in 2θ scan range from 20° to 90°, with a step size of $\Delta(2\theta)$ = 0.04° and a step time of 1 s. The PDF-4+ 2019 software containing the ICDD database was used to index the diffraction patterns.

Microstructural characterization of samples was carried out using a Scanning Electron Microscope (SEM, Hitachi S-3400N) equipped with an Energy Dispersive X-Ray Spectrometer (EDS, Bruker AXS Xflash Detector 5010). Samples for SEM examinations were ground with SiC emery paper up to 4000 grade, polished with diamond paste down to 1 μm and then etched in a Nital solution

(2 vol.% nitric acid and 98 vol.% ethanol) to reveal the microstructure.

TEM foils were prepared using a standard combination of mechanical thinning and ion-beam milling techniques. TEM analysis was conducted using a JEOL JEM 2100HT microscope operating at 200 kV equipped with an EDS (OXFORD INCA) for compositional analysis. The PDF-4+ 2019 software containing the ICDD database was used to determine the crystal system, space group and lattice parameters of the sample. The grain size was determined using the linear intercept method; the average of the measured values was used as the grain size of the alloy.

The volume fraction of the secondary phases was calculated using an image analysis software (LAS V4.8) connected to an optical micrograph (OM, Leica DMR). Six different pictures were used for this calculation.

2.3. Mechanical Properties

The microhardness of the specimens was evaluated using a Microhardness Tester (SHIMADZU HMV-2TE), applying loads of 980.7 mN ($HV_{0.1}$) for 20 s. Ten different indentations were performed in every sample for the average value.

Nanoindentation tests were carried out to determine the hardness and elastic modulus of the different phases in the as-cast Mg-1Zn-1Ca alloy. The tests were performed in a XP Nanoindenter (MTS) with a Berkovich (three sided pyramidal) diamond indenter working in quasi static mode. A load of 2.5 mN was applied for 15 s. A matrix of 625 tests (25 x 25) with a distance of 25 μm between indentations in x- and y-axis was carried out. Afterwards, the indentations were observed by OM and SEM.

The elastic modulus of the studied Mg-based alloy was measured using the continuous stiffness measurement (CSM) method until a penetration depth of 3000 nm, a 5 nm harmonic oscillation amplitude and 45 Hz harmonic frequency. At least, five indentations were performed on different zones of the sample in order to obtain a representative of the elastic modulus for the bulk alloy.

A Deben bending micromachine was installed in a SEM to obtain the load-displacement curves of the samples and simultaneously observe the crack progression until fracture at room temperature. During bending, the flexural strain (ε_f) can be calculated as:

$$\varepsilon_f = \frac{6Dd}{L^2} \quad \text{Eq. 1}$$

where *D* is the maximum deflection of the centre of the substrate, *d* is the height of the sample and *L* is the support span length. The flexural stress (σ_f) was calculated using the following expression:

$$\sigma_f = \frac{3L}{2bd^2}F \quad \text{Eq. 2}$$

F being the maximum load and *b* the width of the tested sample.

The fracture toughness (K_Q) of bent specimens was determined according to the E 399 – 90: *Standard Test Method for Plane-Strain Fracture Toughness of Metallic Materials* [35], using the following equation:

$$K_Q = \left(\frac{P_Q S}{BW^{3/2}}\right) f\left(\frac{a}{W}\right) \quad \text{Eq. 3}$$

Where P_Q is the maximum load, S is the span, B and W are the specimen thickness and width respectively, a is the crack length and $f\left(\frac{a}{W}\right)$ is a defined function.

Load-displacement curves during the bending tests were obtained using a 200 N load cell and a displacement rate of 0.5 mm min^{-1} while the crack-advance was monitored by SEM. Samples of 2.5 x 1 x 30 mm^3 without a pre-crack (Figure 1a) and of 2.5 x 2 x 30 mm^3 (Figure 1b) with a pre-crack of 0.3 mm were used for bending tests using the three-point configuration shown in Figure 1. The area examined by SEM was polished with diamond paste to 1μm and etched in a Nital solution containing 2 vol.% of concentrated nitric acid to observe the fracture pathway through the sample.

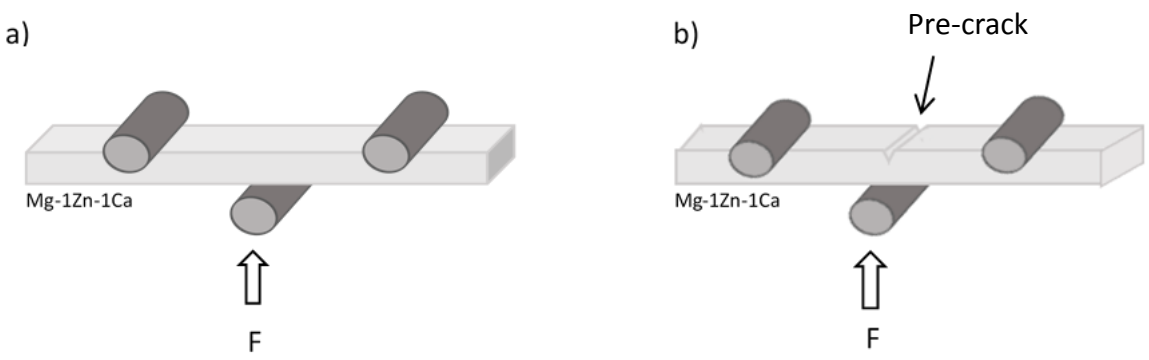

Figure 1. Schematic of the three-point bending tests on samples (a) without and (b) with pre-crack.

2.4. Corrosion Evaluation

Electrochemical tests were carried out in an Autolab PGStat302N potentiostat, provided with Nova 2.1 software, using a three-electrode cell configuration consisting of: a silver/silver chloride (Ag/AgCl, KCl 3M) electrode as the reference electrode, a graphite rod as the counter electrode and the Mg-1Zn-1Ca sample with an exposed area of 0.78 cm^2 as the working electrode. Hank's Balanced Salt Solution (Hank's solution) was used as electrolyte. Before electrochemical testing, samples were ground with 1200 grade SiC emery paper, ultrasonically cleaned in isopropanol for 5 min and dried using hot air.

Linear polarization tests were performed to obtain the polarization resistance of the samples (*Rp*). The scan rate was 1 mV s^{-1} and the applied potential range ± 10 mV from the corrosion potential (E_{corr}). *Rp* values were acquired at time 0 h and after different immersion times (1, 6, 24, 48, 72, 96 and 168 h). Tests were conducted in triplicate.

Anodic-cathodic polarization measurements were carried out polarizating the samples with a potential range from -400 mV to 800 mV relative to the open-circuit potential (*OCP*) and a scanning rate of 1 mV s^{-1}. The corrosion potential (E_{corr}) and the corrosion current density (i_{corr}) were calculated using the Tafel extrapolation method after 1 h of immersion in Hank´s solution. Samples were immersed in Hank's solution until a steady value of *OCP* was reached.

AC Electrochemical Impedance measurements were performed at different immersion times (0, 1, 4, 24, 48, 72, 96 and 168 h) in Hank's solution at room temperature. For it, a sinusoidal potential was applied at the open circuit potential (*OCP*) with an amplitude of 10 mV over the frequency range from 10^5 to 10^{-2} Hz, recording 9 points per decade. The impedance data were analysed using Nyquist and Bode plots. All the electrochemical tests were performed in triplicate to examine the reproducibility of the results.

The set up illustrated in Figure 2 was used to perform the hydrogen evolution tests. Samples were immersed in 125 mL of Hank's solution saturated with hydrogen gas in a thermostatic bath with controlled temperature at 37 °C. Carbon dioxide (CO_2) was bubbled through the solution to maintain a constant pH value of 7.4. Three different specimens were tested to obtain the average value. Corrosion rate P_H (mm y^{-1}) was determined by the hydrogen evolution rate V_H (mL cm^{-2} d^{-1}) using the equation [36]:

$$P_H = 2.279\ V_H \qquad \text{Eq. 4}$$

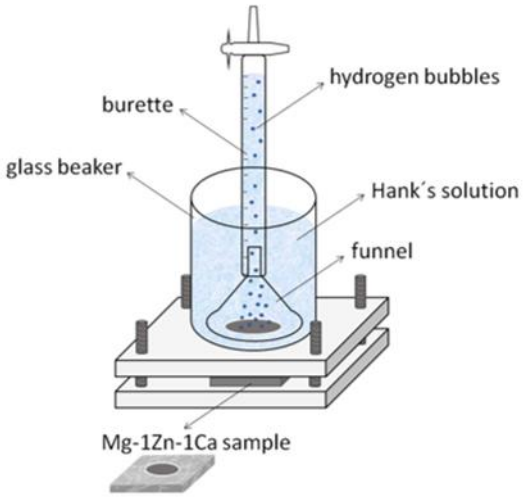

Figure 2. Experimental arrangement for the hydrogen evolution measurements.

Samples of the as-cast Mg-1Zn-1Ca with dimensions of 30 x 20 x 2.5 mm^3 were used in the electrochemical and hydrogen evolution tests. The specimens were ground with 1200 grade SiC emery paper, ultrasonically cleaned in isopropanol for 5 min and dried using hot air.

To determine the corrosion mechanisms after different immersion times in Hank's solution, samples were cleaned with distilled water and the solution of CrO_3 (200 g L^{-1}) and $AgNO_3$ (10 g L^{-1}) to eliminate the corrosion products. The surface morphologies of the specimens were investigated using a Leica S6D stereomicroscope equipped with a Leica DFC320 digital camera. The Zeta-20 3D optical profilometer was used to perform a three-dimensional surface topography analysis of the tested samples. Images were recorded with a z-resolution of 0.5 μm.

To evaluate the corrosion progress through the thickness after 336 h of immersion in Hank's solution, the cross-sections of the tested samples were examined by SEM (Figure 3). Finally, the corrosion products formed during the test were analysed by XRD.

Table 2 shows the chemical composition of the Hank's solution supplied by Sigma-Aldrich and used in this research.

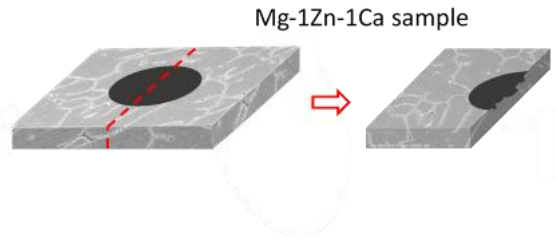

Figure 3. Sample preparation for the observation of the corrosion process.

Table 2. Nominal composition of 1 L of Hank's solution (in g).

$CaCl_2$	$MgSO_4$	KCl	KH_2PO_4	NaCl	Na_2HPO_4	D-Glucose
0.1396	0.09767	0.4	0.06	8.0	0.04788	1.0

3. Results and Discussion

3.1. Composition and Microstructure Characterization

Figure 4 shows the XRD pattern of the as-cast Mg-1Zn-1Ca alloy. As expected, the most intense peaks correspond to the α-Mg matrix phase, which is the main element in the alloy. Peaks with lower intensity were also detected. These peaks are referred to the Mg_2Ca and $Ca_2Mg_6Zn_3$ secondary phases.

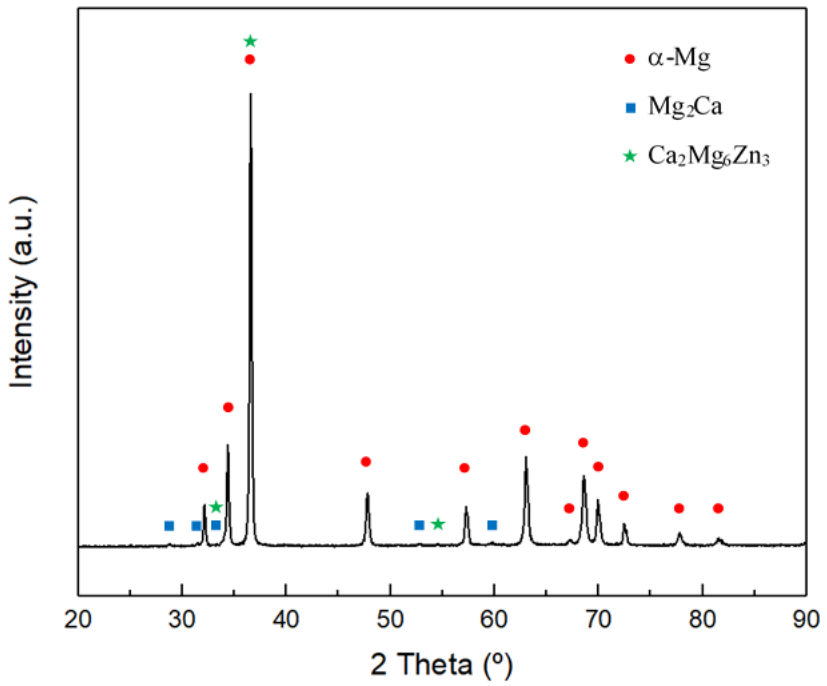

Figure 4. X-Ray diffraction pattern of the as-cast Mg-1Zn-1Ca alloy.

Figure 5a shows the distribution of the secondary phases in the alloy. They are preferentially located at the grain boundaries, leading to continuous networks through the entire volume of the sample [37]. Figure 5b, showing a magnification in SEM-BSE mode of a grain boundary, shows the presence of two different phases based on their different contrast (one is observed as white particles, while the other one is as dark particles). The compositional analysis of this area (Figure 5c) reveals that the particles at the GBs contain Ca and Zn. Table 3 shows the percentage of each element in the two different secondary phases. As the solubility of Ca and Zn in Mg is 1.35 wt.% and 6.2 wt.% [38], respectively, the formation of intermetallic compounds as precipitates mainly at grain boundaries is promoted, remaining a very small content of such elements within the grains, essentially constituted of α-Mg phase. The results obtained by EDS show that white particles contain Ca and Zn, while the dark ones contain only Ca, which is in agreement with the presence of both Mg_2Ca and $Ca_2Mg_6Zn_3$ particles. Therefore, at the GB there are two different precipitated phases: Mg_2Ca precipitates, which are nearly equiaxial, and

$Ca_2Mg_6Zn_3$ precipitates, which are more elongated and embraced the Mg_2Ca precipitates (Figure 5b).

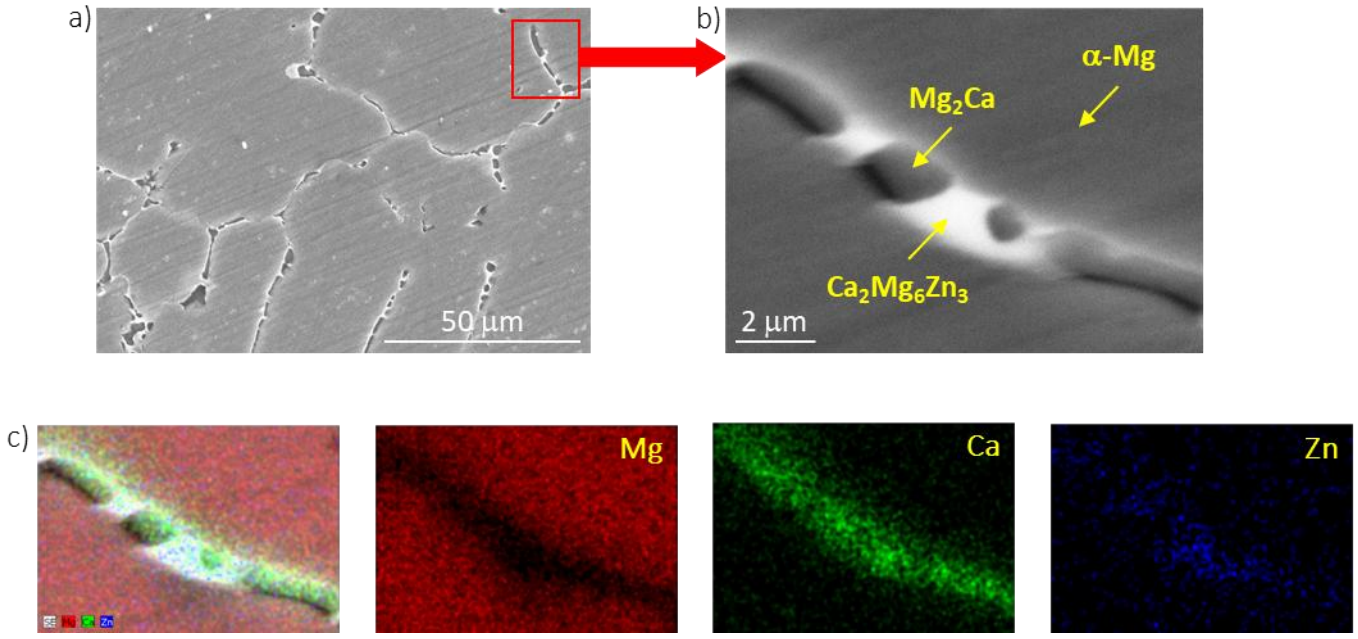

Figure 5. a) SEM-SE micrograph of the as-cast Mg-1Zn-1Ca alloy; b) detailed SEM-BSE image of one grain boundary; c) EDS mapping analysis of the area shown in Fig 5b.

Table 3. EDS compositional analysis of the dark and white particles found at the grain boundaries.

Phase	**Mg (wt. %)**	**Ca (wt. %)**	**Zn (wt. %)**
Dark particles	77.1 ± 4.7	16.4 ± 0.6	6.5 ± 0.5
White particles	61.9 ± 4.2	13.5 ± 0.6	24.7 ± 1.6

TEM examinations of the as-cast Mg-1Zn-1Ca alloy were also performed (Figure 6). The EDS carried out on the matrix shows that basically consists of Mg, while Zn and Ca were mainly distributed into the secondary phases in the alloy. As shown in Figures 6b and 6c, several particles were found in the Mg-1Zn-1Ca alloy, placed preferably at grain boundaries ($Ca_2Mg_6Zn_3$ and Mg_2Ca). When the $Ca_2Mg_6Zn_3$ phase appears at grain boundary, its morphology is larger than within the

grains (as seen in Figure 6b), as reported in literature [39]. The Mg_2Ca intermetallic phase is bean shaped and its proportion in the alloy is lower than the $Ca_2Mg_6Zn_3$ phase. The crystal system of both stable intermetallic compounds is hexagonal as the α-Mg phase. $Ca_2Mg_6Zn_3$ has the space group $P6_3/mmc$ and the lattice parameters a = b = 0.973 nm and c = 1.015 nm. For Mg_2Ca, the space group is $P6_3/mmc$ and the corresponding lattice parameters are a = b = 0.624 nm and c = 1.015 nm. The ICDD database was used to obtain these results. The low solubility of Ca in the Mg matrix originates the aggregation of this element on the grain boundaries, forming the Mg_2Ca and $Ca_2Mg_6Zn_3$ secondary phases. It has been reported the effect of Ca and Zn additions on the grain size: they produce grain refinement in Mg alloys. The Mg-1Zn-1Ca alloy presents an average grain size of 67 ± 3 μm [40–42]. Summarizing, TEM examinations confirm the presence of Mg_2Ca and $Ca_2Mg_6Zn_3$ secondary phases at GBs and $Ca_2Mg_6Zn_3$ particles (in a smaller proportion) within the grains.

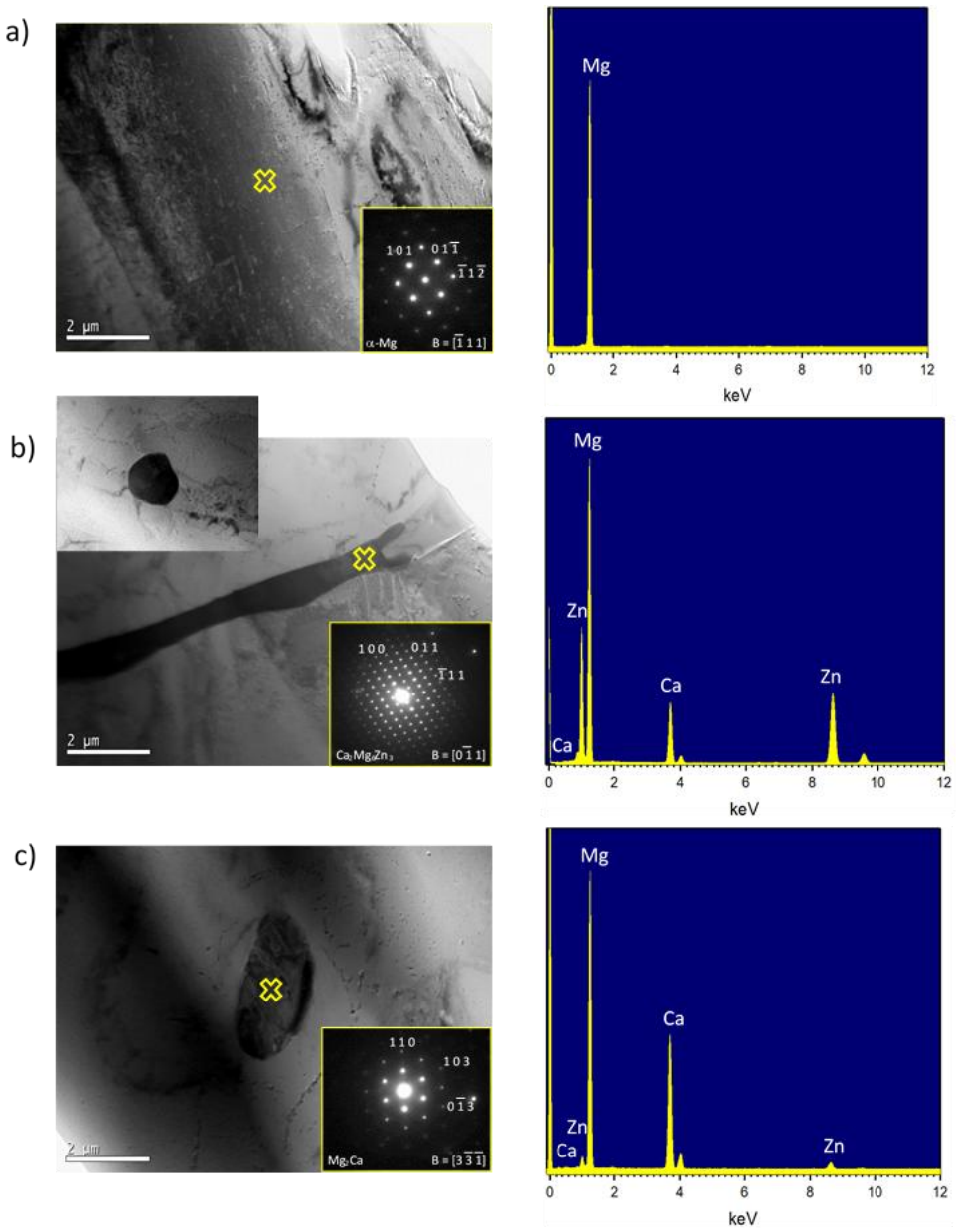

Figure 6. TEM images, electron diffraction patterns and EDS analysis of the as-cast Mg-1Zn-1Ca alloy: a) α-Mg, b) $Ca_2Mg_6Zn_3$ and c) Mg_2Ca.

The volume fraction of both the Mg_2Ca and the $Ca_2Mg_6Zn_3$ phases in the as-cast Mg-1Zn-1Ca alloy was calculated by image analysis. The result was 1.33 ± 0.17 vol.% and 1.45 ± 0.25 vol.%, respectively. These results show that secondary phases represent approximately the 3 vol.% of the as-cast Mg-1Zn-1Ca alloy.

3.2. Hardness and elastic modulus measurements

The mean microhardness at room temperature of the as-cast Mg-1Zn-1Ca alloy was determined to be 61.7 ± 5.7 $HV_{0.1}$, which is higher than that of pure Mg and other Mg-Zn-Ca alloys produced by casting [26,43–45]. It could be attributed to grain refinement and hardening effect of precipitates [46].

Figure 7 represents the nanohardness distribution in the as-cast Mg-1Zn-1Ca alloy. The comparison of the contour map (Figure 7a) and the OM picture (Figure 7b) suggests that the highest hardness values correspond to areas densely populated with secondary phases (mainly GBs), while the lowest ones correspond to the regions within the grains. In agreement, those regions close to the intermetallic compounds show intermediate hardness values. It is important to note that since it was not possible to determine the contribution of each individual secondary phase to the hardness values, the results were treated as a mixed contribution of both phases. The relatively high solubility of zinc at elevated temperatures produces a strengthening effect in the magnesium through a solid solution hardening mechanism [47].

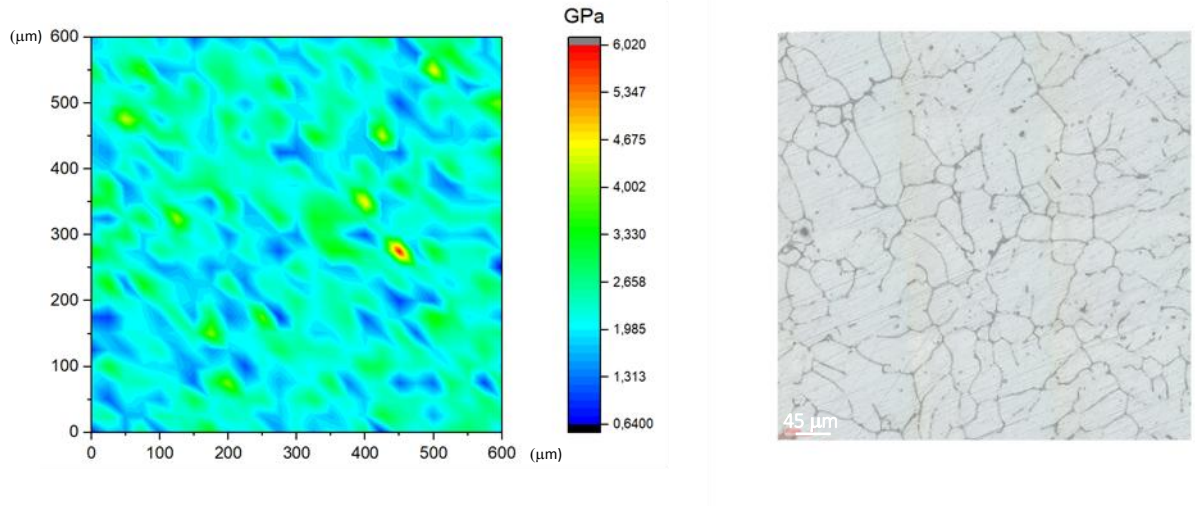

Figure 7. (a) Contour map showing the nanohardness distribution in the as-cast Mg-1Zn-1Ca alloy; (b) OM picture of the area shown in Figure 7a.

The SEM picture in Figure 8a shows three different nanoindentations performed in the as-cast Mg-1Zn-1Ca alloy. The load-displacement curves obtained by the nanoindentation test at these three locations are shown in Figure 8b. The hardness and elastic modulus values calculated from these curves are summarized in Table 4. As expected, location 2, corresponding to a GB populated with secondary phases, gives the highest hardness and elastic modulus values, while location 1, corresponding to a precipitate-free area within a grain, shows the lowest values. In contrast, location 3, within a grain, but close to an intermetallic compound exhibits intermediate values for hardness and elastic modulus. This shows the influence of the secondary phases, which are harder and stiffer, on these mechanical properties of the surrounding α-Mg matrix. Note that the curve corresponding to the indentation 2 shows some discontinuities (indicated with a green arrow) that could be related to relaxation mechanism associated with cracking of the brittle secondary phases during loading, an indication of their brittleness.

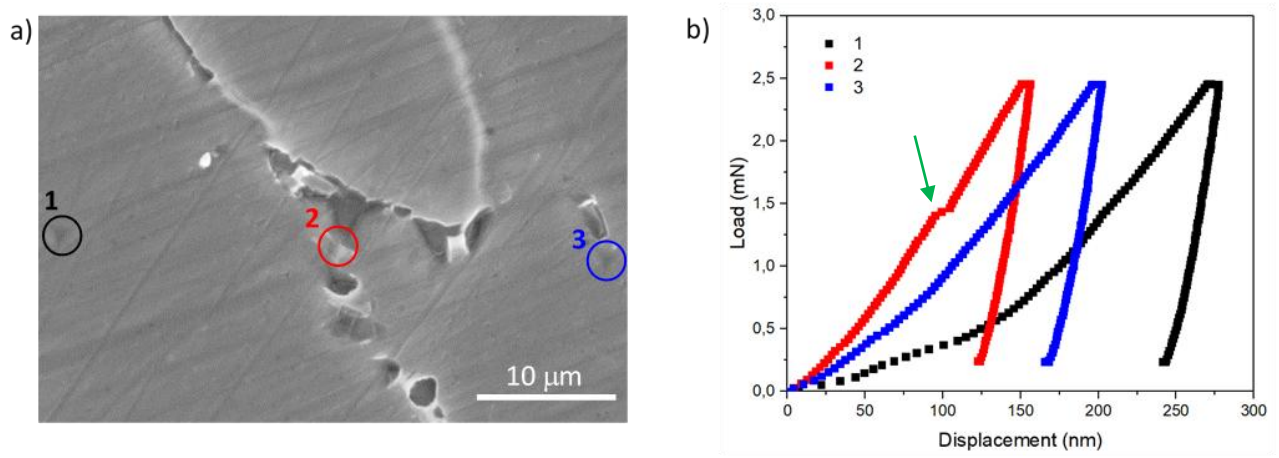

Figure 8. a) SEM-SE micrograph showing three different nanoindentations; b) load-displacement curves corresponding to these three locations.

Table 4. Hardness and elastic modulus values obtained from the load-displacement curves in Figure 8b.

Location	Hardness (GPa)	Elastic modulus at maximum load (GPa)
1	1.3	56.6
2	4.5	121.6
3	2.6	85.7

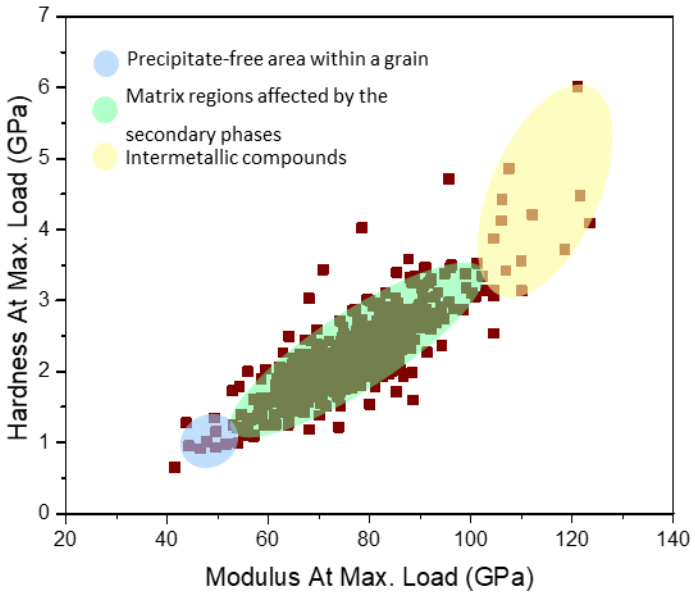

Figure 9. Relationship between nanoindentation hardness and elastic modulus at maximum load.

Figure 9 represents the nanoindentation hardness versus the nanoindentation elastic modulus at all the tested points. It is patent that those areas in the matrix far from intermetallic precipitates exhibit hardness and indentation modulus values ranging from 0.5 - 1.5 GPa and 40 - 60 GPa, respectively. In contrast, the hardness values for the intermetallic compounds are in the range between 3.3 and 6.0 GPa, with the elastic modulus varying from 95 to 125 GPa. Finally, intermediate hardness and elastic modulus values correspond to the matrix regions affected by the secondary phases. The intermetallic compounds show superior resistant properties (hardness and strength) that involves lower ductility and fracture toughness. It should be noted that hardness values obtained for all phases are overestimated due to the influence of the indentation size effect.

The nanoindentation measurements evidence that the different phases have distinct values of hardness and elastic modulus and the macroscopic values observed for the alloy are de combination of the mechanical behaviour of the different phases. In this alloy the presence and distribution of the intermetallic precipitates cause an increase of hardness and elastic modulus compared to the α-Mg phase.

Figure 10 shows the evolution of the elastic modulus with the displacement into the surface for the studied alloy at five different positions. At low depths there was hardening due to the indentation size effect, becoming the elastic modulus stable at higher depths. An average elastic modulus of 54.4 ± 2.4 GPa was obtained for indentations from 1000 to 3000 nm in-depth. This value is similar to those previously reported for a similar alloy and it is slightly higher than other values found in literature for biomedical Mg-Zn-Ca and Mg-Zn-Al-Ca alloys produced by casting [16,48]. It is worth-mentioning that the present as-cast Mg-1Zn-1Ca alloy shows an elastic modulus more similar to that of the bone (3 – 20 GPa) than titanium alloys (110 – 117 GPa) or stainless steel (189 – 210 GPa) [3,49] do. This indicates the good compatibility of the studied Mg-1Zn-1Ca alloy and its potential to be used in biodegradable implants with an elastic modulus that is associated to the presence and distribution of intermetallic phases in the alloy.

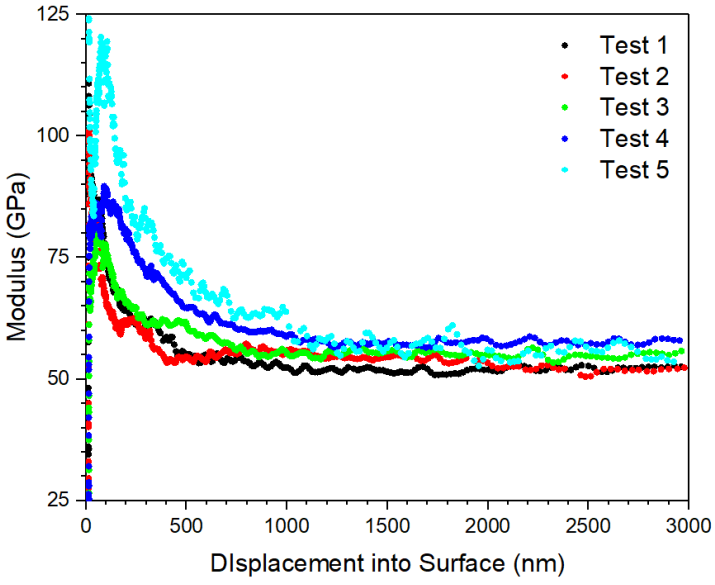

Figure 10. Modulus in-depth results at five different positions in the as-cast Mg-1Zn-1Ca alloy.

3.3. Three-point Bending Test and Mechanism

In-situ bending tests were also performed on the as-cast Mg-1Zn-1Ca alloy. Figure 11a shows that cracks initially nucleate on the surface in tension and grow towards the opposite surface (see red arrows). Figure 11b shows the front of the main crack, which apparently propagates through the GBs. This could be attributed to the brittleness of the secondary phases, preferentially located at the GBs, which could provide an easy path for cracks, giving rise to brittle intergranular fracture. Low ductility and fast crack propagation are characteristic of this type of fracture. Figure 11b also suggests the nucleation of secondary cracks at the GBs (see green arrows). They may create alternative paths for crack propagation. As observed in Figure 11c, the two parts of the sample after breakage are complementary, being negligible the plastic deformation. Moreover, in most cases, there are intermetallic compounds remaining at both edges of the fracture across the entire volume of the sample (see yellow arrows). Finally, Figure 11d displays the schematic representation of the complete fracture process: a) initiation of the crack, b) propagation and apparition of secondary cracks and c) fracture of the specimen.

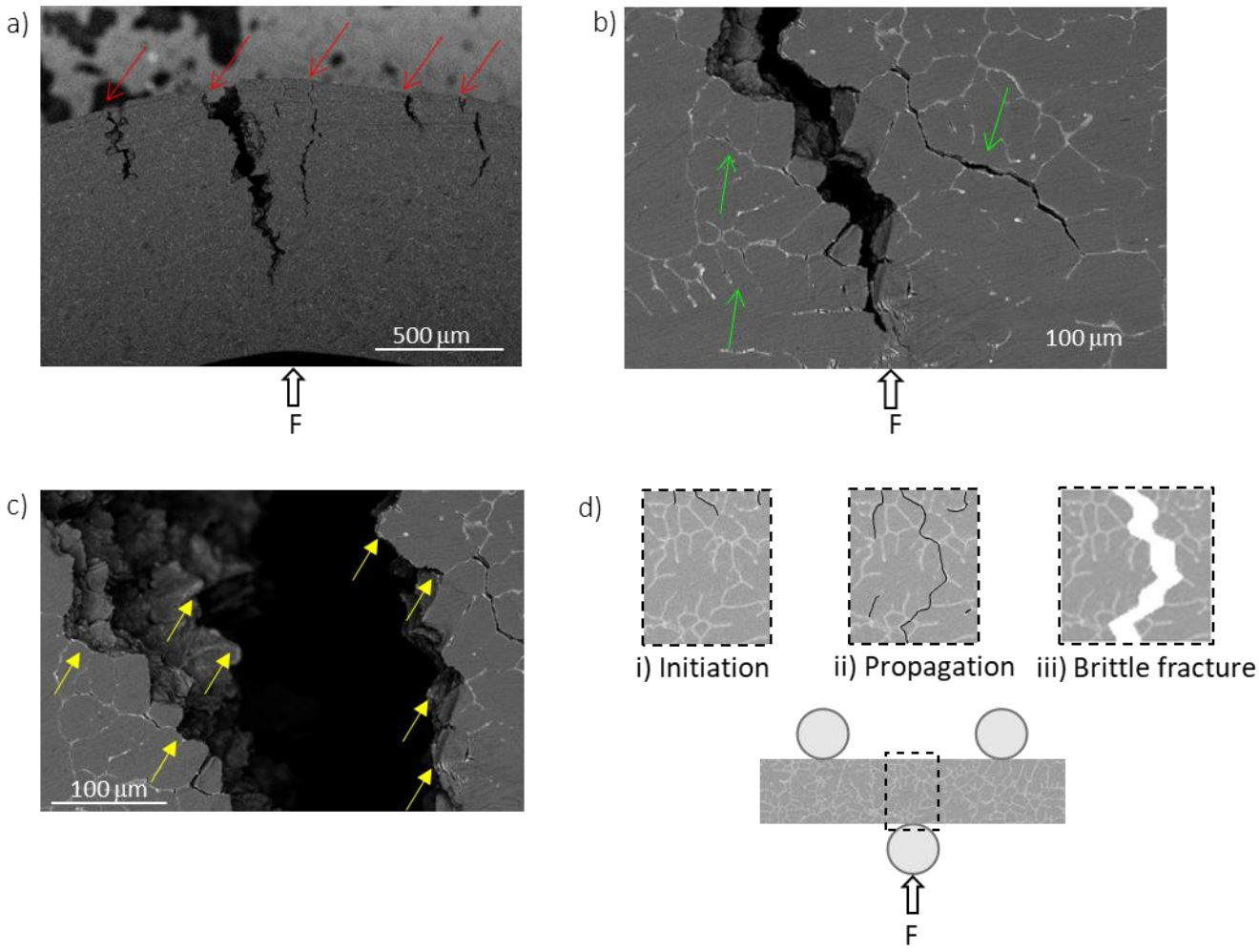

Figure 11. a) Crack initiation and propagation in the as-cast Mg-1Zn-1Ca alloy during the three-point bending tests; b) Front of the main crack and secondary cracks; c) SEM-BSE micrograph of the brittle fracture mechanism of Mg_2Ca and $Ca_2Mg_6Zn_3$ distributed at grain boundaries. The red arrows identify the nucleation of initial cracks, the green arrows identify the secondary cracks at the GBs and the yellow arrows identify the secondary phases at the edge of the fracture.

Figure 12 shows the load-displacement curves corresponding to bending tests performed on the as-cast Mg-1Zn-1Ca alloy. Flexural strain and stress were determined from the curves corresponding to samples without a pre-crack (Figure 12a). Values of 10.14 ± 1.90 % and 96 ± 3 MPa were obtained for the flexural strain and flexural stress, respectively. These results agree with the values obtained by other authors for Mg-based alloys used for biomedical applications [6].

As observed, upon loading, the intermetallic precipitates will show much less strain than the α-Mg grains and this, combined with the elongated geometry of the precipitated particles, results in the concentration of stress at the intermetallic precipitated phases. For this reason, the crack initiates in the secondary phases and have a preferential path along them. The continuous network formed by these intermetallic compounds facilitates the crack progression across the samples producing the fracture of the specimen in a small period of time. The strength and the toughness of the alloy are linked to the volume fraction, composition, morphology and distribution of the secondary phases, and the crack evolution images and model proposed evidence that it is considered as the key factor of the limited toughness of the alloy. On the other hand, the existence of hard phases in the alloy increases the hardness and strength of the alloy, particularly in compression conditions, but may result in low toughness values.

Fracture toughness of the as-cast Mg-1Zn-1Ca alloy was calculated from the curves corresponding to samples with a pre-crack (Figure 12b). A mean value of 4.95 ± 0.19 MPa $m^{1/2}$ was calculated, which is within the range of the natural bone (3-6 MPa $m^{1/2}$) [5,50] and lower than those measured for other Mg-based alloys (7 to 20 MPa $m^{1/2}$) [51–53]. This low value is consistent with the brittle fracture mode. On the one hand, it is favoured by the brittleness of the intermetallic phases that present higher hardness than the matrix (Table 4) and also much higher elastic modulus (Figure 10); on the other hand, their preferential location at the GBs forming a continuous network combined with the elongated geometry of the particles (Figures 5 and 11) results in the concentration of stress at the intermetallic precipitated phases that provides a crack propagation pathway.

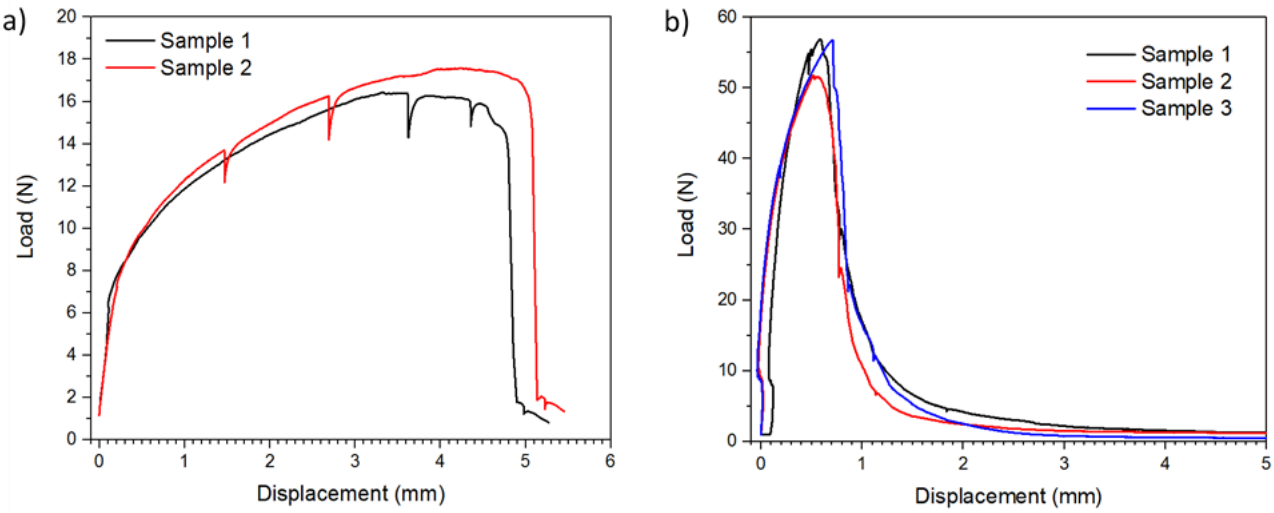

Figure 12. Load-displacement curves from three-point bending tests: a) without pre-crack and b) with pre-crack (discontinuities in the curves correspond to the breaks done during the tests to obtain in-situ images of the cracks).

3.4. Corrosion Behaviour

The polarization resistance (*Rp*) of the as-cast Mg-1Zn-1Ca alloy after different immersion times in Hank's solution is shown in Figure 13a. The maximum values of *Rp* were achieved for times between 6 and 24 h. After 24 h of immersion in the electrolyte, the *Rp* and thus the corrosion resistance of the Mg-based alloy decreases with increasing the immersion time. After 72 h of immersion, the *Rp* reaches a constant value, suggesting a steady state in the corrosion mechanisms of the alloy.

The anodic-cathodic curves of the as-cast Mg-1Zn-1Ca alloy after 1 h of immersion in Hank's solution are shown in Figure 13b. From these curves a corrosion potential (E_{corr}) of -1.62 V was calculated for the alloy. This value agrees with those found for Mg alloys in the literature [7], always reporting an electrochemical potential below -1.40 V due to the limited solubility of most elements in pure Mg. The mean current density was 4.39 ± 0.81 μA cm^{-2}.

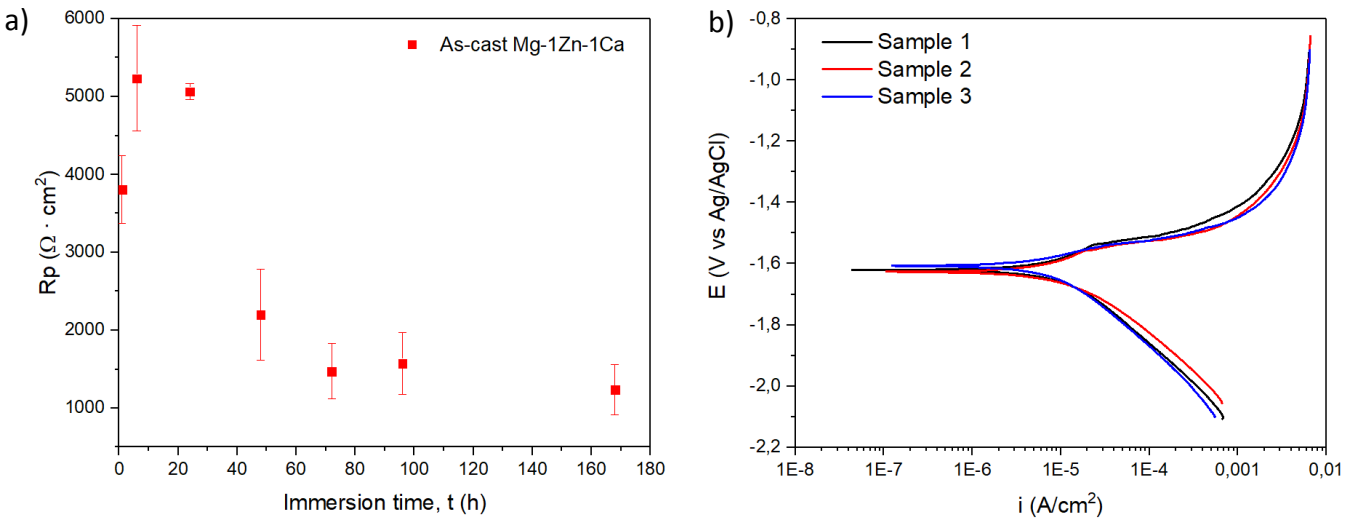

Figure 13. a) Polarization resistance (Rp) as a function of the immersion time in Hank's solution and b) Anodic-cathodic curves for the as-cast Mg-1Zn-1Ca alloy.

Figure 14 shows the Nyquist and Bode diagrams of the EIS measurements for the as-cast Mg-1Zn-1Ca alloy for up to 336 h of immersion in Hank's solution. During the long-term EIS measurement, the EIS spectra displayed two different types of behaviour. The equivalent circuits used to fit the experimental data are shown in Figure 15, where R_e is the resistance of the electrolyte, R_f and CPE_f are introduced because of the formation of the $Mg(OH)_2$ passive layer during surface stabilization in *OCP* [54], R_{cp} and CPE_{cp} are the resistance and the capacitive behaviour of the corrosion products formed on the alloy surface and R_{ct} and CPE_{dl} describe the charge transfer resistance and the capacitance of the double layer corresponding to the electrochemical activities in the substrate/electrolyte interface. *L* was introduced take into account the inductive behaviour and it indicates the existence of the metastable Mg^+ during magnesium alloy substrate dissolution [55]. The EIS fitting parameters obtained for the as-cast Mg-1Zn-1Ca alloy after different immersion times are listed in Table 5.

The Nyquist plots for the corrosion of the Mg-1Zn-1Ca alloy in Hank's solution at the different immersion times studied (1 h, 4 h, 24 h, 48 h, 72 h, 96 h and 168 h) are displayed in Figure

14a. The capacitive loop observed at the high frequency region is attributed to the charge transfer reaction in the electric double layer formed at the interface between the Mg surface and the electrolyte and the medium-frequency time constant is associated with the mass transport in solid phase, as the diffusion processes through the corrosion products layer. These two relaxation processes are sometimes difficult to distinguish because of a strong overlapping. At low frequencies, the inductive loop could be ascribed to the relaxation of adsorbed species on the metal surface or to the dissolution of the semi-passive corrosion product film [56–58]. For 1 h, 4 h and 24 h of immersion times in Hank's solution, an additional relaxation process associated to the formation of a $Mg(OH)_2$ passive layer appeared. As observed in Figure 14b, corresponding to the Bode plot, for these immersion times, i.e., up to 24 – 48 h, the modulus of impedance grows. However, after 48 h of immersion time it decreased. Hank's solution is considered as an aggressive media due to the high Cl^- ions concentration. These ions are able to convert the $Mg(OH)_2$ layer into $MgCl_2$, which is easily dissolved in the Hank's solution [59]. For this reason, after 48 h of immersion, the corrosion accelerates and results in the disappearance of the film resistance of the coating (R_f), which implies a change in the equivalent circuit of the corrosion system from that of Figure 15a to the simpler one shown in figure 15b. This behaviour is also in accordance with the *Rp* results obtained by the linear polarization tests (Figure 13a).

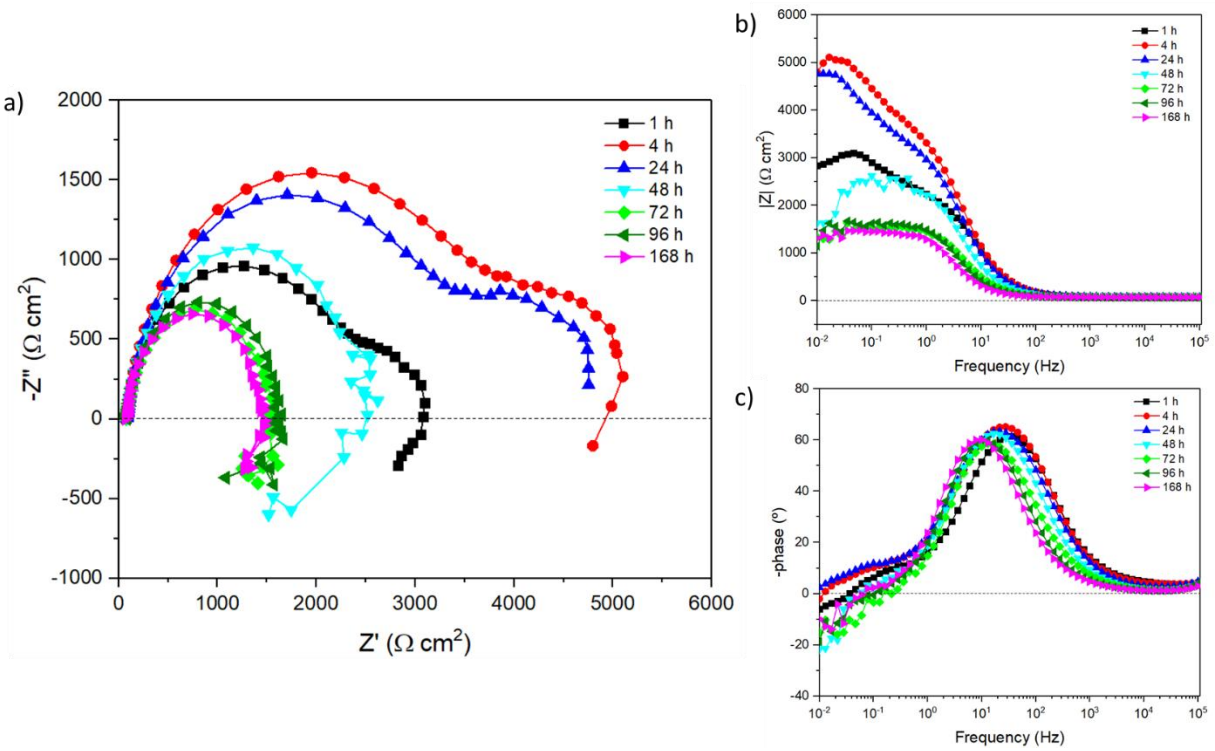

Figure 14. a) Nyquist and b) and c) Bode plots of the EIS spectra for the corrosion of Mg-1Zn-1Ca alloy at different immersion times in Hank's solution.

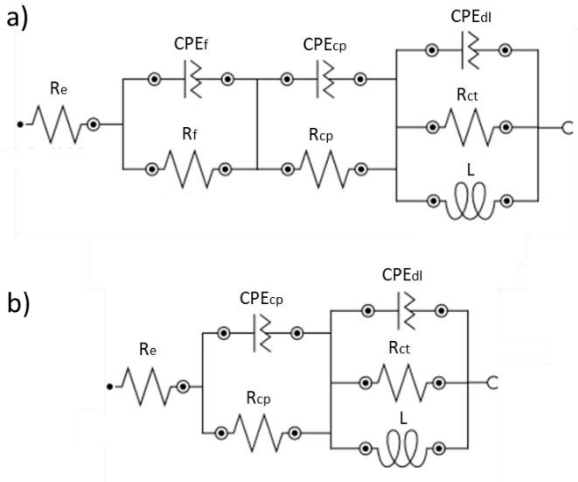

Figure 15. Equivalent electrical circuit models used to simulate the impedance spectra: a) 1h, 4h and 24 h and b) 48 h, 72h, 96 h and 168 h of immersion time in Hank's solution at room temperature.

Table 5. EIS simulated resistance values of as-cast Mg-1Zn-1Ca alloy.

Immersion time (h)	R_e (Ω cm^2)	R_f (Ω cm^2)	R_{cp} (Ω cm^2)	R_{ct} (Ω cm^2)
1	72.9	615.4	1769.6	1011.2
4	73.9	1406.2	3886.8	1287.7
24	78.8	1477.3	4052.7	1129.7
48	78.5	-	1177.1	1058.6
72	73.5	-	602.0	869.0
96	79.8	-	713.4	853.2
168	72.2	-	693.6	709.4

Figure 16 shows the hydrogen volume evolution data as a function of immersion time in Hank's solution at 37 °C for the as-cast Mg-1Zn-1Ca alloy. It can be seen that the volume of hydrogen increases with increasing the immersion time in Hank's solution. However, two different corrosion stages could be defined: one from the beginning to 160 h and another one from 160 h to 336 h. The present experimental data fit well to the following linear equation: $V = V_H \cdot t + b$, where V is the volume of hydrogen (mL cm^{-2}) and t is the immersion time (h). The corrosion rate (P_H) corresponding to each interval was obtained using Eq. 4, the values being 0.60 mm y^{-1} for the first stage (P_{H1}) and 3.17 mm y^{-1} for the second one (P_{H2}). The first stage, with a lower corrosion rate, is related to the initial period of corrosion of the alloy when it is in direct contact with the electrolyte. Exceeding

160 h of immersion, the corrosion process accelerates. The second stage, however, is ascribed to a change in the corrosion mechanism from general to localized corrosion after long immersion times. Erinc et al. [60] established a value of 0.50 mm y^{-1} as the maximum corrosion rate acceptable for

implant biomaterials working in direct contact with simulated body fluid at 37 °C. For the as-cast Mg-1Zn-1Ca alloy, until 160 h of immersion in Hank's solution, the result is close to this limit value.

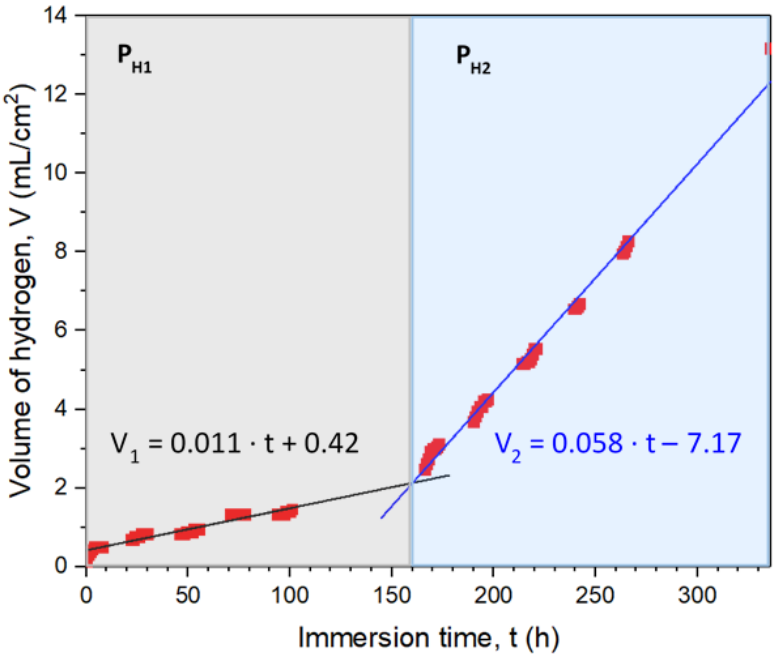

Figure 16. Representation of hydrogen volume versus immersion time in Hank's solution, showing two different corrosion stages.

It is important to note that the volume of evolved hydrogen for the present Mg-1Zn-1Ca alloy is lower than that previously observed for other Mg alloys. D. Song et al. [61] reported that after

70 h of immersion in Hank's solution, the hydrogen evolution of a Mg-Zn-Ca alloy was higher than 10 mL cm^{-2}. F. Zhang et al. [62] studied the hydrogen evolution rate of high-purity Mg and two different Mg alloys: Mg-Zn-Mn-Ca and Mg-Zn-Mn-Ca-Ce, obtaining for the three cases a value equal or higher than 20 mL cm^{-2} after 240 h of immersion. Finally, for the widely used AZ91 alloy, C. Taltavull et al. [63] showed values higher than 4 mL cm^{-2} after 168 h of immersion in Hank's solution, while N. I. Zainal Abidin et al. [64] reported values of 1.43 mm y^{-1} and 7.16 mm y^{-1} after 240 h of testing.

The profilometry technique has been used to study the change of the dominant corrosion

mechanism with immersion time (Figure 17). Figures 17a, 17b and 17c are referred to the surface morphologies after 72 h of immersion and Figures 17d, 17e and 17f correspond to the sample after 336 h of immersion. The surface in Figure 17a presents a more homogeneously corroded surface compared to that in Figure 17d, where localized corrosion is visible. To analyse the corrosion evolution, depth profiles (Figures 17b and 17e) were made across the tested region of the samples. After 72 h of immersion (Figure 17b), the height remains almost constant, with a small variation of ~ 20 μm, showing a uniform corrosion mechanism in the tested area. However, in Figure 17e, the difference in height is up to 350 μm and it is non-uniform throughout the scanned area. It indicates the existence of localized corrosion. The 3D images (Figures 17c and 17f) also show the change in the corrosion mechanism depending on the immersion time.

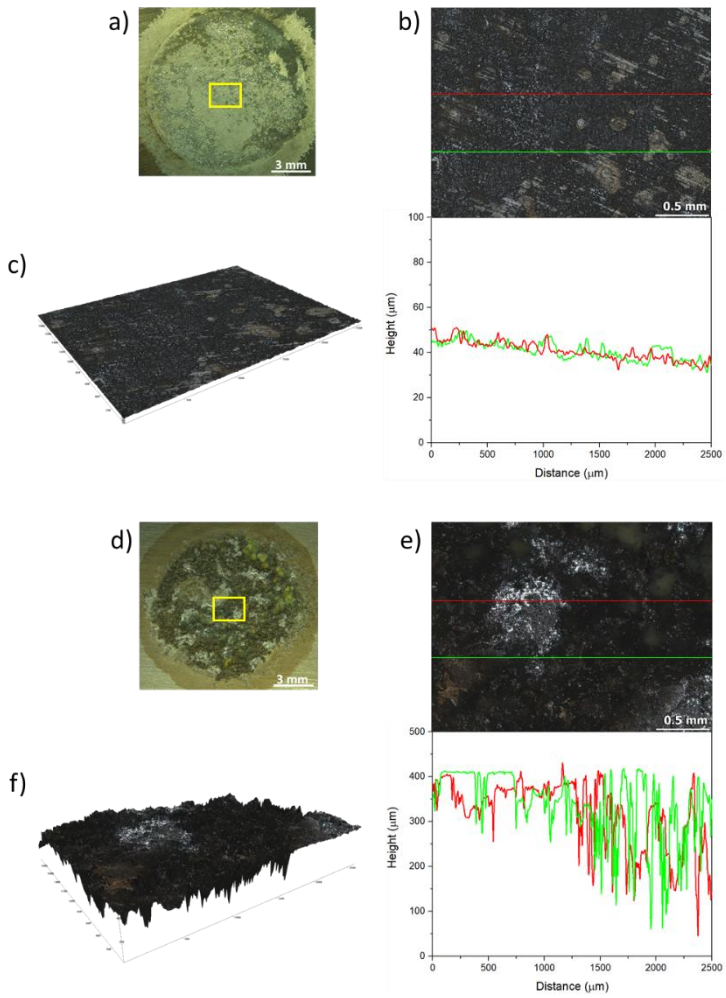

Figure 17. Surface images of the samples after a) 72 h and d) 336 h of immersion in Hank's solution; b) and e) Magnifications of yellow boxed areas in a) and d) and their corresponding profilometry data; c) and f) 3D images.

Figure 18 shows SEM images of the as-cast Mg-1Zn-1Ca alloy after 336 h of immersion in Hank's solution. SEM inspections on the cross-section of the same sample (Figure 18a) show evidences of general corrosion. These observations suggest that the sample is mainly corroded by general corrosion followed by localized corrosion, which is consistent with the acceleration of the corrosion rate after 160 h of immersion time (Figure 16) and the profilometry results (Figure 17). Pits are anodic areas in the sample which are smaller than the cathodic ones. This promotes a faster corrosion process.

In addition, closer inspections of the corroded area (Figures 19b and 19c) reveal that corrosion in the alloy takes place through the α-Mg matrix. This, in turn, suggests that the Mg_2Ca and $Ca_2Mg_6Zn_3$ intermetallic compounds act as barriers against corrosion, blocking the advance of the corrosion. This appears to be contradictory because, according to the electrochemical potential of the different phases (Mg_2Ca < α-Mg < $Ca_2Mg_6Zn_3$), corrosion should mainly start at the Mg_2Ca precipitates [65]. However, in the studied microstructure, $Ca_2Mg_6Zn_3$ is embracing the Mg_2Ca phase because of the casting route used. Therefore, Mg_2Ca is not in contact with the electrolyte and the only galvanic pair formed is between $Ca_2Mg_6Zn_3$ and the α-Mg matrix. This causes that the dissolution starts at the matrix but is not galvanically promoted because of the low exposed area of the intermetallic precipitate. As this secondary phase may have continuity faults, or after its breakage, the process starts again in a grain beneath the former one. This effect is due to the combined presence of the two intermetallic phases involved, and particularly to the presence and distribution of the $Ca_2Mg_6Zn_3$ precipitates around the Mg_2Ca ones. In the absence of the $Ca_2Mg_6Zn_3$ precipitates, the mechanism would have consisted in the degradation of the phases

present at grain boundaries and the separation of the α-Mg grains from the bulk. The effect of these secondary phases acting as a local barrier against corrosion due to the continuous network formed in the alloy is more dominant than the electrochemical potential of the phases.

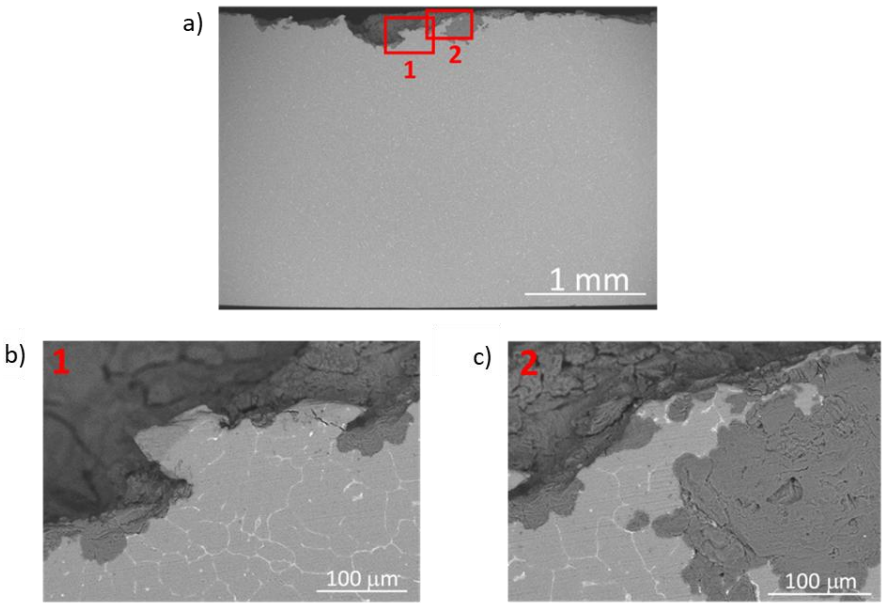

Figure 18. SEM-SE pictures of the as-cast Mg-1Zn-1Ca alloy after 336 h of immersion in Hank's solution. a) Cross-section; b) and c) Magnifications of areas 1 and 2 in Figure 18a.

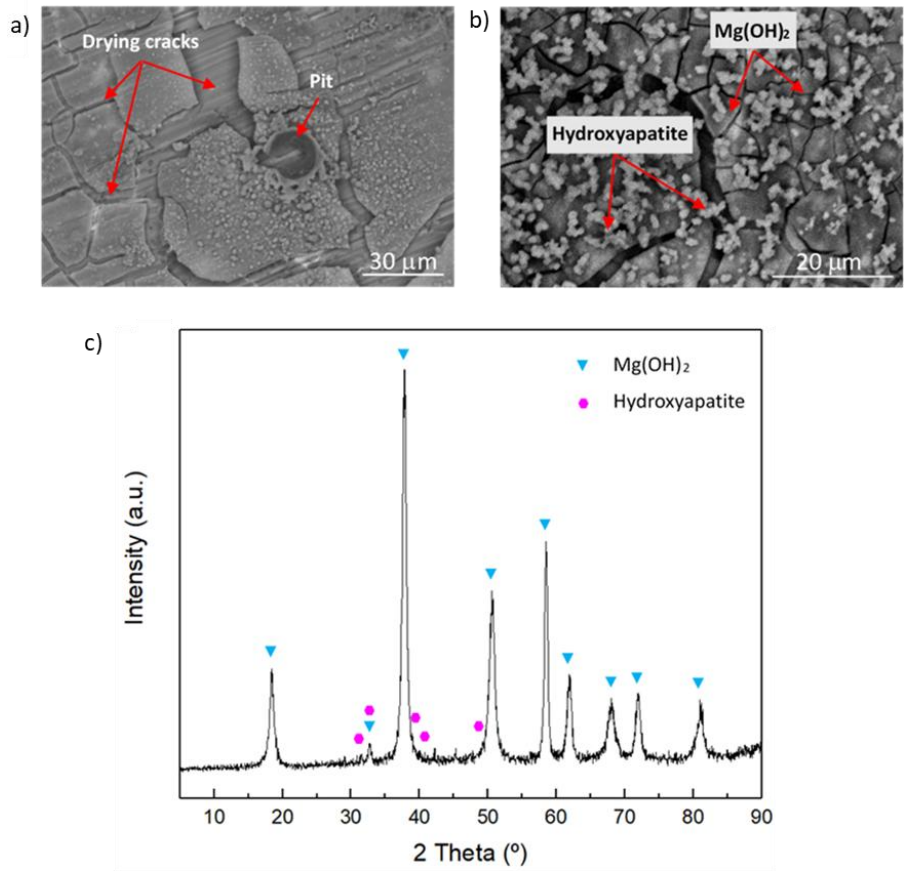

Figure 19. a) and b) SEM-BSE images and c) X-Ray diffraction pattern of the corrosion products formed in the as-cast Mg-1Zn-1Ca alloy after 336 h of immersion in Hank's solution at 37 °C.

High-magnification SEM pictures of the surface in contact with the Hank's solution at 37 °C after 336 h of immersion are shown in Figures 19a and 19b. Figure 19a shows a small cavity on the top surface that indicates a change in the corrosion mechanism from general to localized. In Figure 19b, the corrosion products formed on surface can be observed: $Mg(OH)_2$ and hydroxyapatite.

When a sample is immersed in Hank's solution, the high concentration of chloride ions (Cl^-) in solution constitutes the principal factor causing the corrosion. The composition of the main corrosion products was determined by the XRD technique (Figure 19c). The most intense peaks correspond to magnesium hydroxide, $Mg(OH)_2$, forming a continuous and protective layer on the alloy surface, which reduces the corrosion rate of the alloy. The thickness and compaction of the

$Mg(OH)_2$ depends on the immersion time [67]. Corrosion of Mg and its alloys causes the alkalinisation of the media, increasing the tendency to generate a $Mg(OH)_2$ film. However, the presence of Cl^- ions and the hydrogen bubbles formed during Mg immersion can produce the breakdown of this protective layer in local areas, leading to localized corrosion and an accelerated corrosion of the Mg matrix. In agreement with previous works [68–70], other visible peaks in the XRD spectra correspond to hydroxyapatite, showing the stimulatory effect of Mg on the bone healing and formation of new bone tissue. Hydroxyapatite is formed on the $Mg(OH)_2$ passive layer, that presents several cracks due to the drying after immersion test (Figures 20a and 20b) [71,72]. This explains that despite the amount of corrosion products increases with increasing the immersion time, the corrosion resistance of the alloy reaches a steady state (Figure 13a).

Figure 20 shows a schematic of the corrosion mechanism in the as-cast Mg-1Zn-1Ca alloy when it is immersed in Hank's solution. Figure 20a shows the first stage of the corrosion process, which consists of the uniform dissolution of the alloy and the formation of a thin protective layer on the exposed area. However, this passive layer is broken locally by the Cl^- ions and the hydrogen bubbles generated, and small pits, which leave small areas of the alloy in direct contact with the electrolyte, appear (Figure 20b). It is further promoted by the galvanic couple between the α-Mg matrix and the intermetallic secondary phases. In this case, the intermetallic phase present does not dissolve, as has been indicated before in the analysis of the electrochemical behaviour of the alloy, but it contributes to the dissolution of the α-Mg grain. Then, the continuous phase present at the grain boundary provides some resistance to the corrosion progression slowing down the corrosion process. Once the matrix is dissolved and the solution meets the intermetallic compounds (Figure 20d), corrosion can only proceed through the discontinuities in the network formed by the secondary phases. Finally, corrosion takes place through the α-Mg matrix by a localized corrosion mechanism (Figure 20c) that increases the progression of the corrosion of the alloy.

The combination of free Mg^{2+} and Ca^{2+} cations with the phosphates in solution gives rise to the formation of hydroxyapatite on the remaining protective $Mg(OH)_2$ layer (Figure 20d), which is promoted by the pH raise caused by the presence of OH^- in solution.

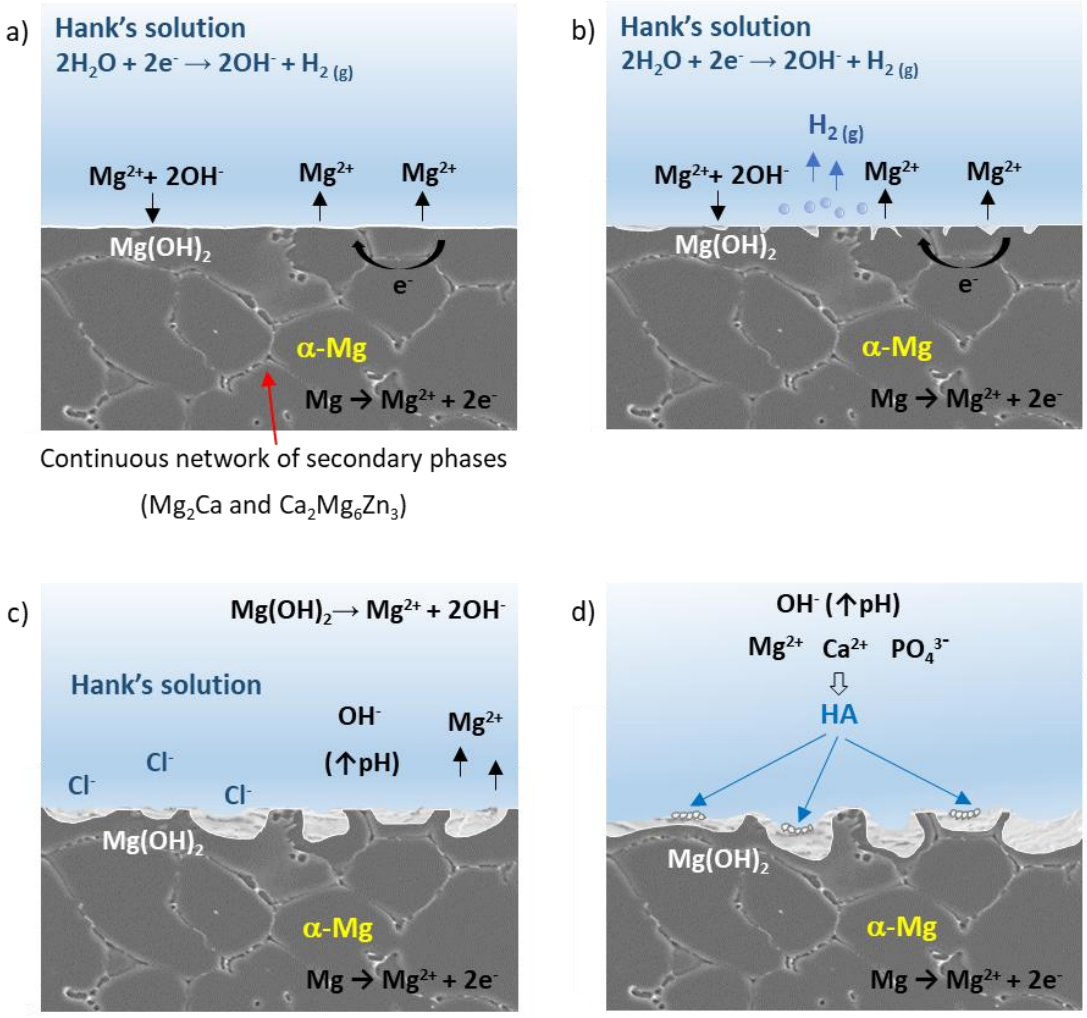

Figure 20. Corrosion mechanism in the as-cast Mg-1Zn-1Ca alloy in Hank's solution: a) uniform corrosion and formation of a protective layer; b) formation of the first pits; c) localized corrosion; d) precipitation of hydroxyapatite on the protective layer.

4. Conclusions

In this research, the microstructure and composition of an as-cast Mg-1Zn-1Ca alloy have been deeply studied. In addition, the mechanical properties and the corrosion mechanism have

been investigated in order to determine the suitability of this alloy to be used in biodegradable implants.

The following conclusions can be drawn:

1) The as-cast Mg-1Zn-1Ca alloy contains Mg_2Ca and $Ca_2Mg_6Zn_3$ intermetallic particles. They locate preferentially at the GBs forming a continuous network and the $Ca_2Mg_6Zn_3$ phase surrounds the Mg_2Ca one.
2) The Mg_2Ca and $Ca_2Mg_6Zn_3$ phases show higher hardness and stiffness than the matrix, providing a higher hardness magnesium alloy.
3) During flexural test, fracture cracks initiate at the intermetallic precipitates because of the difference in hardness between them and the matrix, and due to the concentration of stress at the precipitates placed on the surface of the sample. Then cracks propagate through the continuous network formed by the intermetallic compounds at grain boundaries. For this reason the as-cast alloy shows a brittle fracture mechanism.
4) The galvanic pair formed between the intermetallic phases causes the dilution of the α-Mg phase because the nobler $Ca_2Mg_6Zn_3$ phase surrounds the more active Mg_2Ca one. This causes an initial uniform corrosion of the alloy in Hank´s solution. Afterwards, the corrosion progress through the α-Mg phase following a localized corrosion mechanism, degrading its properties with time. The stable intermetallic compounds act as a barrier against corrosion, which forces the corrosion to progress through the discontinuities in the secondary phase network.
5) During immersion, a protective layer of $Mg(OH)_2$ is formed over the surface of the alloy and hydrogen gas is evolved. The degradation of the as-cast Mg-1Zn-1Ca alloy in contact to Hank's solution also promotes the precipitation of hydroxyapatite.

Acknowledgements

The authors would like to acknowledge the financial support from the Agencia Estatal de Investigación (Project RTI2018-096391-B-C31), Comunidad de Madrid (Project ADITIMAT-CM S2018/NMT-4411) and the FPU grant (15/03606) from the Ministerio de Educación, Cultura y Deporte, Spain.

References

[1] W. Li, S. Guan, J. Chen, J. Hu, S. Chen, L. Wang, S. Zhu, Preparation and in vitro degradation of the composite coating with high adhesion strength on biodegradable Mg-Zn-Ca alloy, Mater. Charact. 62 (2011) 1158–1165. https://doi.org/10.1016/j.matchar.2011.07.005.

[2] M. Ali, M.A. Hussein, N. Al-Aqeeli, Magnesium-based composites and alloys for medical applications: A review of mechanical and corrosion properties, J. Alloys Compd. 792 (2019) 1162–1190. https://doi.org/10.1016/j.jallcom.2019.04.080.

[3] G. Song, Control of biodegradation of biocompatable magnesium alloys, Corros. Sci. 49 (2007) 1696–1701. https://doi.org/10.1016/j.corsci.2007.01.001.

[4] H.R.B. Rad, M.H. Idris, M.R.A. Kadir, S. Farahany, A. Fereidouni, M.Y. Yahya, Characterization and corrosion behavior of biodegradable Mg-Ca and Mg-Ca-Zn implant alloys, in: Appl. Mech. Mater., 2012: pp. 568–572. https://doi.org/10.4028/www.scientific.net/AMM.121-126.568.

[5] M.P. Staiger, A.M. Pietak, J. Huadmai, G. Dias, Magnesium and its alloys as orthopedic biomaterials: A review, Biomaterials. 27 (2006) 1728–1734. https://doi.org/10.1016/j.biomaterials.2005.10.003.

[6] J. Chen, L. Tan, X. Yu, I.P. Etim, M. Ibrahim, K. Yang, Mechanical properties of magnesium alloys for medical application: A review, J. Mech. Behav. Biomed. Mater. 87 (2018) 68–79. https://doi.org/10.1016/j.jmbbm.2018.07.022.

[7] K. Gusieva, C.H.J. Davies, J.R. Scully, N. Birbilis, Corrosion of magnesium alloys: the role of alloying, Int. Mater. Rev. 60 (2015) 169–194. https://doi.org/10.1179/1743280414Y.0000000046.

[8] X. Gu, Y. Zheng, Y. Cheng, S. Zhong, T. Xi, In vitro corrosion and biocompatibility of binary magnesium alloys, Biomaterials. 30 (2009) 484–498. https://doi.org/10.1016/j.biomaterials.2008.10.021.

[9] H.R. Bakhsheshi-Rad, E. Hamzah, A. Fereidouni-Lotfabadi, M. Daroonparvar, M.A.M.M. Yajid, M. Mezbahul-Islam, M. Kasiri-Asgarani, M. Medraj, Microstructure and bio-corrosion behavior of Mg-Zn and Mg-Zn-Ca alloys for biomedical applications, Mater. Corros. 65 (2014) 1178–1187. https://doi.org/10.1002/maco.201307588.

[10] D. Zander, N.A. Zumdick, Influence of Ca and Zn on the microstructure and corrosion of biodegradable Mg-Ca-Zn alloys, Corros. Sci. 93 (2015) 222–233. https://doi.org/10.1016/j.corsci.2015.01.027.

[11] H. Li, Q. Peng, X. Li, K. Li, Z. Han, D. Fang, Microstructures, mechanical and cytocompatibility of degradable Mg-Zn based orthopedic biomaterials, Mater. Des. 58 (2014) 43–51. https://doi.org/10.1016/j.matdes.2014.01.031.

[12] H.R. Bakhsheshi-Rad, M.R. Abdul-Kadir, M.H. Idris, S. Farahany, Relationship between the corrosion behavior and the thermal characteristics and microstructure of Mg-0.5Ca-xZn alloys, Corros. Sci. 64 (2012) 184–197. https://doi.org/10.1016/j.corsci.2012.07.015.

[13] S.A. Abdel-Gawad, M.A. Shoeib, Corrosion studies and microstructure of Mg−Zn−Ca alloys for biomedical applications, Surfaces and Interfaces. 14 (2019) 108–116. https://doi.org/10.1016/j.surfin.2018.11.011.

[14] R. Radha, D. Sreekanth, Insight of magnesium alloys and composites for orthopedic implant applications – a review, J. Magnes. Alloy. 5 (2017) 286–312. https://doi.org/10.1016/j.jma.2017.08.003.

[15] L. Katsarou, K. Suresh, K.P.P. Rao, N. Hort, C. Blawert, C.L.L. Mendis, H. Dieringa, Microstructure and properties of magnesium alloy Mg-1Zn-1Ca (Zx11), 2015. https://doi.org/10.1007/978-3-319-48185-2_78.

[16] B. Zhang, Y. Hou, X. Wang, Y. Wang, L. Geng, Mechanical properties, degradation performance and cytotoxicity of Mg-Zn-Ca biomedical alloys with different compositions, Mater. Sci. Eng. C. 31 (2011) 1667–1673. https://doi.org/10.1016/j.msec.2011.07.015.

[17] S.M. Baek, H.K. Park, J.I. Yoon, J. Jung, J.H. Moon, S.G. Lee, J.H. Kim, T.S. Kim, S. Lee, N.J. Kim, H.S. Kim, Effect of secondary phase particles on the tensile behavior of Mg-Zn-Ca alloy, Mater. Sci. Eng. A. 735 (2018) 288–294. https://doi.org/10.1016/j.msea.2018.08.050.

[18] H.X. Wang, S.K. Guan, X. Wang, C.X. Ren, L.G. Wang, In vitro degradation and mechanical integrity of Mg-Zn-Ca alloy coated with Ca-deficient hydroxyapatite by the pulse electrodeposition process, Acta Biomater. 6 (2010) 1743–1748. https://doi.org/10.1016/j.actbio.2009.12.009.

[19] D.W.H. Kim, B.C. Suh, M.S. Shim, J.H. Bae, D.W.H. Kim, N.J. Kim, Texture evolution in Mg-Zn-Ca alloy sheets, Metall. Mater. Trans. A Phys. Metall. Mater. Sci. 44 (2013) 2950–2961. https://doi.org/10.1007/s11661-013-1674-2.

[20] Y. Ortega, T. Leguey, R. Pareja, Tensile fracture behavior of aging hardened Mg-1Ca and Mg-1Ca-1Zn alloys, Mater. Lett. 62 (2008) 3893–3895. https://doi.org/10.1016/j.matlet.2008.05.021.

[21] X. Gao, S.M. Zhu, B.C. Muddle, J.F. Nie, Precipitation-hardened Mg-Ca-Zn alloys with superior creep resistance, Scr. Mater. 53 (2005) 1321–1326. https://doi.org/10.1016/j.scriptamat.2005.08.035.

[22] M. Bamberger, G. Levi, J.B. Vander Sande, Precipitation hardening in Mg-Ca-Zn alloys, Metall. Mater. Trans. A Phys. Metall. Mater. Sci. 37 (2006) 481–487. https://doi.org/10.1007/s11661-006-0019-9.

[23] N. Li, Y. Zheng, Novel Magnesium Alloys Developed for Biomedical Application: A Review, J. Mater. Sci. Technol. 29 (2013) 489–502. https://doi.org/10.1016/j.jmst.2013.02.005.

[24] K.P. Rao, K. Suresh, Y.V.R.K. Prasad, C. Dharmendra, N. Hort, H. Dieringa, High temperature strength and hot working technology for As-cast Mg-1Zn-1Ca (ZX11) alloy, Metals (Basel). 7 (2017). https://doi.org/10.3390/met7100405.

[25] Y. Jang, Z. Tan, C. Jurey, Z. Xu, Z. Dong, B. Collins, Y. Yun, J. Sankar, Understanding corrosion

behavior of Mg-Zn-Ca alloys from subcutaneous mouse model: Effect of Zn element concentration and plasma electrolytic oxidation, Mater. Sci. Eng. C. 48 (2015) 28–40. https://doi.org/10.1016/j.msec.2014.11.029.

[26] H. Ibrahim, A.D. Klarner, B. Poorganji, D. Dean, A.A. Luo, M. Elahinia, Microstructural, mechanical and corrosion characteristics of heat-treated Mg-1.2Zn-0.5Ca (wt%) alloy for use as resorbable bone fixation material, J. Mech. Behav. Biomed. Mater. 69 (2017) 203–212. https://doi.org/10.1016/j.jmbbm.2017.01.005.

[27] R.C. Zeng, W.C. Qi, H.Z. Cui, F. Zhang, S.Q. Li, E.H. Han, In vitro corrosion of as-extruded Mg-Ca alloys-The influence of Ca concentration, Corros. Sci. 96 (2015) 23–31. https://doi.org/10.1016/j.corsci.2015.03.018.

[28] P.R. Cha, H.S. Han, G.F. Yang, Y.C.Y.Y.C. Kim, K.H. Hong, S.C. Lee, J.Y. Jung, J.P. Ahn, Y.C.Y.Y.C. Kim, S.Y. Cho, J.Y. Byun, K.S. Lee, S.J. Yang, H.K. Seok, Biodegradability engineering of biodegradable Mg alloys: Tailoring the electrochemical properties and microstructure of constituent phases, Sci. Rep. 3 (2013) 1–6. https://doi.org/10.1038/srep02367.

[29] F. Naghdi, R. Mahmudi, J.Y. Kang, H.S. Kim, Microstructure and high-temperature mechanical properties of the Mg-4Zn-0.5Ca alloy in the as-cast and aged conditions, Mater. Sci. Eng. A. 649 (2016) 441–448. https://doi.org/10.1016/j.msea.2015.10.011.

[30] Y.Z. Du, X.G. Qiao, M.Y. Zheng, D.B. Wang, K. Wu, I.S. Golovin, Effect of microalloying with Ca on the microstructure and mechanical properties of Mg-6 mass%Zn alloys, Mater. Des. 98 (2016) 285–293. https://doi.org/10.1016/j.matdes.2016.03.025.

[31] Y. Sun, B. Zhang, Y. Wang, L. Geng, X. Jiao, Preparation and characterization of a new biomedical Mg-Zn-Ca alloy, Mater. Des. 34 (2012) 58–64. https://doi.org/10.1016/j.matdes.2011.07.058.

[32] V. Roche, G.Y. Koga, T.B. Matias, C.S. Kiminami, C. Bolfarini, W.J. Botta, R.P. Nogueira, A.M. Jorge Junior, Degradation of biodegradable implants: The influence of microstructure and

composition of Mg-Zn-Ca alloys, J. Alloys Compd. 774 (2019) 168–181. https://doi.org/10.1016/j.jallcom.2018.09.346.

[33] Y.Z. Du, M.Y. Zheng, C. Xu, X.G. Qiao, K. Wu, X.D. Liu, G.J. Wang, X.Y. Lv, Microstructures and mechanical properties of as-cast and as-extruded Mg-4.50Zn-1.13Ca (wt%) alloys, Mater. Sci. Eng. A. 576 (2013) 6–13. https://doi.org/10.1016/j.msea.2013.03.034.

[34] F.R. Elsayed, N. Hort, M.A. Salgado Ordorica, K.U. Kainer, Magnesium Permanent Mold Castings Optimization, Mater. Sci. Forum. 690 (2011) 65–68. https://doi.org/10.4028/www.scientific.net/msf.690.65.

[35] R. Documents, S. Factor, P.F. Toughness, Standard Test Method for Plane-Strain Fracture Toughness of Metallic Materials 1, Configurations. 90 (1997) 1–31. https://doi.org/10.1520/E0399-09E02.2.

[36] Z. Shi, A. Atrens, An innovative specimen configuration for the study of Mg corrosion, Corros. Sci. 53 (2011) 226–246. https://doi.org/10.1016/j.corsci.2010.09.016.

[37] W. jian Li, K. kun Deng, X. Zhang, K. bo Nie, F. jun Xu, Effect of ultra-slow extrusion speed on the microstructure and mechanical properties of Mg-4Zn-0.5Ca alloy, Mater. Sci. Eng. A. 677 (2016) 367–375. https://doi.org/10.1016/j.msea.2016.09.059.

[38] M. Němec, A. Jäger, K. Tesař, V. Gärtnerová, Influence of alloying element Zn on the microstructural, mechanical and corrosion properties of binary Mg-Zn alloys after severe plastic deformation, Mater. Charact. 134 (2017) 69–75. https://doi.org/10.1016/j.matchar.2017.10.017.

[39] T. Zhou, M. Yang, Z. Zhou, J. Hu, Z. Chen, Microstructure and mechanical properties of rapidly solidified/powder metallurgy Mg-6Zn and Mg-6Zn-5Ca at room and elevated temperatures, J. Alloys Compd. 560 (2013) 161–166. https://doi.org/10.1016/j.jallcom.2013.01.066.

[40] X. LUO, D. FANG, Q. LI, Y. CHAI, Microstructure and mechanical properties of an Mg-4.0Sm-

1.0Ca alloy during thermomechanical treatment, J. Rare Earths. 34 (2016) 1134–1138. https://doi.org/10.1016/S1002-0721(16)60145-X.

[41] H.B. Li, G.C. Yao, Z.Q. Guo, Y.H. Liu, H.J. Yu, H.B. Ji, Microstructure and mechanical properties of Mg-Li with Ca addition, 19 (2006) 355–361.

[42] A. Zakiyuddin, K. Lee, Effect of a small addition of zinc and manganese to Mg-Ca based alloys on degradation behavior in physiological mediaEffect of a small addition of zinc and manganese to Mg-Ca based alloys on degradation behavior in physiological media, J. Alloys Compd. 629 (2015) 274–283. https://doi.org/10.1016/j.jallcom.2014.12.181.

[43] K. Kubok, L. Litynska-Dobrzynska, A. Wierzbicka-Miernik, J. Wojewoda-Budka, Age hardening of Mg-3Zn-xCa (x = 0, 0.5, 1.0) wt.% alloys, in: Mater. Sci. Forum, 2013: pp. 481–485. https://doi.org/10.4028/www.scientific.net/MSF.765.481.

[44] B. Langelier, A. Korinek, P. Donnadieu, S. Esmaeili, Improving precipitation hardening behavior of Mg-Zn based alloys with Ce-Ca microalloying additions, Mater. Charact. 120 (2016) 18–29. https://doi.org/10.1016/j.matchar.2016.08.010.

[45] K. Oh-ishi, R. Watanabe, C.L. Mendis, K. Hono, Age-hardening response of Mg-0.3 at.%Ca alloys with different Zn contents, Mater. Sci. Eng. A. 526 (2009) 177–184. https://doi.org/10.1016/j.msea.2009.07.027.

[46] Q. Kang, H. Jiang, Y. Zhang, Z. Xu, H. Li, Z. Xia, Effect of various Ca content on microstructure and fracture toughness of extruded Mg-2Zn alloys, J. Alloys Compd. 742 (2018) 1019–1030. https://doi.org/10.1016/j.jallcom.2017.11.276.

[47] S. Zhang, X. Zhang, C. Zhao, J. Li, Y. Song, C. Xie, H. Tao, Y. Zhang, Y. He, Y. Jiang, Y. Bian, Research on an Mg-Zn alloy as a degradable biomaterial, Acta Biomater. 6 (2010) 626–640. https://doi.org/10.1016/j.actbio.2009.06.028.

[48] B. Homayun, A. Afshar, Microstructure, mechanical properties, corrosion behavior and cytotoxicity of Mg-Zn-Al-Ca alloys as biodegradable materials, J. Alloys Compd. 607 (2014)

1–10. https://doi.org/10.1016/j.jallcom.2014.04.059.

[49] Y. Lu, A.R. Bradshaw, Y.L. Chiu, I.P. Jones, Effects of secondary phase and grain size on the corrosion of biodegradable Mg-Zn-Ca alloys, Mater. Sci. Eng. C. 48 (2015) 480–486. https://doi.org/10.1016/j.msec.2014.12.049.

[50] F. Libonati, L. Vergani, Bone toughness and crack propagation: An experimental study, Procedia Eng. 74 (2014) 464–467. https://doi.org/10.1016/j.proeng.2014.06.298.

[51] V. Kaushik, R. Narasimhan, R.K. Mishra, Experimental study of fracture behavior of magnesium single crystals, Mater. Sci. Eng. A. 590 (2014) 174–185. https://doi.org/10.1016/j.msea.2013.10.018.

[52] H. Somekawa, T. Mukai, Effect of grain refinement on fracture toughness in extruded pure magnesium, Scr. Mater. 53 (2005) 1059–1064. https://doi.org/10.1016/j.scriptamat.2005.07.001.

[53] B. Kim, J. Do, S. Lee, I. Park, In situ fracture observation and fracture toughness analysis of squeeze cast AZ51-xSn magnesium alloys, Mater. Sci. Eng. A. 527 (2010) 6745–6757. https://doi.org/10.1016/j.msea.2010.07.016.

[54] Z.U. Rahman, K.M. Deen, W. Haider, Controlling corrosion kinetics of magnesium alloys by electrochemical anodization and investigation of film mechanical properties, Appl. Surf. Sci. 484 (2019) 906–916. https://doi.org/10.1016/j.apsusc.2019.02.168.

[55] Y. Song, D. Shan, R. Chen, F. Zhang, E.H. Han, Biodegradable behaviors of AZ31 magnesium alloy in simulated body fluid, Mater. Sci. Eng. C. 29 (2009) 1039–1045. https://doi.org/10.1016/j.msec.2008.08.026.

[56] B. Torres, E. Otero, J. Rams, Surface & Coatings Technology Corrosion behavior of 316L stainless steel coatings on ZE41 magnesium alloy in chloride environments, Surf. Coat. Technol. 378 (2019) 124994. https://doi.org/10.1016/j.surfcoat.2019.124994.

[57] G. Galicia, N. Pébère, B. Tribollet, V. Vivier, Local and global electrochemical impedances

applied to the corrosion behaviour of an AZ91 magnesium alloy, Corros. Sci. 51 (2009) 1789–1794. https://doi.org/10.1016/j.corsci.2009.05.005.

[58] M. Mohedano, B.J.C. Luthringer, B. Mingo, F. Feyerabend, R. Arrabal, P.J. Sanchez-Egido, C. Blawert, R. Willumeit-Römer, M.L. Zheludkevich, E. Matykina, Bioactive plasma electrolytic oxidation coatings on Mg-Ca alloy to control degradation behaviour, Surf. Coatings Technol. 315 (2017) 454–467. https://doi.org/10.1016/j.surfcoat.2017.02.050.

[59] N.M. Chelliah, P. Padaikathan, R. Kumar, Evaluation of electrochemical impedance and biocorrosion characteristics of as-cast and T4 heat treated AZ91 Mg-alloys in Ringer ' s solution, J. Magnes. Alloy. 7 (2019) 134–143. https://doi.org/10.1016/j.jma.2019.01.005.

[60] M. Erinc, W.H. Sillekens, R.G.T.M. Mannens, R.J. Werkhoven, Applicability of existing magnesium alloys as biomedical implant materials, Magnes. Technol. (2009) 209–214. https://doi.org/10.1017/CBO9781107415324.004.

[61] D. Song, G. Guo, J. Jiang, L. Zhang, A. Ma, X. Ma, J. Chen, Z. Cheng, Hydrothermal synthesis and corrosion behavior of the protective coating on Mg-2Zn-Mn-Ca-Ce alloy, Prog. Nat. Sci. Mater. Int. 26 (2016) 590–599. https://doi.org/10.1016/j.pnsc.2016.11.002.

[62] F. Zhang, A. Ma, D. Song, J. Jiang, F. Lu, L. Zhang, D. Yang, J. Chen, Improving in-vitro biocorrosion resistance of Mg-Zn-Mn-Ca alloy in Hank's solution through addition of cerium, J. Rare Earths. 33 (2015) 93–101. https://doi.org/10.1016/S1002-0721(14)60388-4.

[63] C. Taltavull, Z. Shi, B. Torres, J. Rams, A. Atrens, Influence of the chloride ion concentration on the corrosion of high-purity Mg, ZE41 and AZ91 in buffered Hank's solution, J. Mater. Sci. Mater. Med. 25 (2014) 329–345. https://doi.org/10.1007/s10856-013-5087-y.

[64] N.I. Zainal Abidin, A.D.A. Atrens, D. Martin, A.D.A. Atrens, Corrosion of high purity Mg, Mg2Zn0.2Mn, ZE41 and AZ91 in Hank's solution at 37°C, Corros. Sci. 53 (2011) 3542–3556. https://doi.org/10.1016/j.corsci.2011.06.030.

[65] N.T. Kirkland, N. Birbilis, J. Walker, T. Woodfield, G.J. Dias, M.P. Staiger, In-vitro dissolution of

magnesium-calcium binary alloys: Clarifying the unique role of calcium additions in bioresorbable magnesium implant alloys, J. Biomed. Mater. Res. - Part B Appl. Biomater. 95 (2010) 91–100. https://doi.org/10.1002/jbm.b.31687.

[66] N. Sezer, Z. Evis, S. Murat, A. Tahmasebifar, M. Koç, S.M. Kayhan, A. Tahmasebifar, M. Koç, Review of magnesium-based biomaterials and their applications, J. Magnes. Alloy. 6 (2018) 23–43. https://doi.org/10.1016/j.jma.2018.02.003.

[67] X. Zhang, G. Yuan, L. Mao, J. Niu, P. Fu, W. Ding, Effects of extrusion and heat treatment on the mechanical properties and biocorrosion behaviors of a Mg-Nd-Zn-Zr alloy, J. Mech. Behav. Biomed. Mater. 7 (2012) 77–86. https://doi.org/10.1016/j.jmbbm.2011.05.026.

[68] Z. Li, X. Gu, S. Lou, Y. Zheng, The development of binary Mg-Ca alloys for use as biodegradable materials within bone, Biomaterials. 29 (2008) 1329–1344. https://doi.org/10.1016/j.biomaterials.2007.12.021.

[69] Y.F. Zheng, X.N. Gu, F. Witte, A. Eliezer, Biodegradable metals, Degrad. Implant Mater. 9781461439 (2012) 93–109. https://doi.org/10.1007/978-1-4614-3942-4_5.

[70] S. Zhang, J. Li, Y. Song, C. Zhao, X. Zhang, C. Xie, Y. Zhang, H. Tao, Y. He, Y. Jiang, Y. Bian, In vitro degradation, hemolysis and MC3T3-E1 cell adhesion of biodegradable Mg-Zn alloy, Mater. Sci. Eng. C. 29 (2009) 1907–1912. https://doi.org/10.1016/j.msec.2009.03.001.

[71] D. Mei, S. V. Lamaka, J. Gonzalez, F. Feyerabend, R. Willumeit-Römer, M.L. Zheludkevich, The role of individual components of simulated body fluid on the corrosion behavior of commercially pure Mg, Corros. Sci. 147 (2019) 81–93. https://doi.org/10.1016/j.corsci.2018.11.011.

[72] J. Wang, Y. Ma, S. Guo, W. Jiang, Q. Liu, Effect of Sr on the microstructure and biodegradable behavior of Mg–Zn–Ca-Mn alloys for implant application, Mater. Des. 153 (2018) 308–316. https://doi.org/10.1016/j.matdes.2018.04.062.